Published in final edited form as:
Nat Chem Biol. 2021 April 01; 17(4): 438–447. doi:10.1038/s41589-021-00753-2.

Palmitoylated acyl protein thioesterase APT2 deforms membranes to extract substrate acyl chains

Laurence Abrami[#1], **Martina Audagnotto**[#2], **Sylvia Ho**[1], **Maria Jose Marcaida**[2], **Francisco S. Mesquita**[1], **Muhammad U. Anwar**[1], **Patrick A. Sandoz**[1,4], **Giulia Fonti**[2], **Florence Pojer**[3], **Matteo Dal Peraro**[2,*], **F. Gisou van der Goot**[1,*]

[1]Global Health Institute, School of Life Sciences, EPFL, Lausanne, Switzerland [2]Institute of Bioengineering, School of Life Sciences, EPFL, Lausanne, Switzerland [3]Protein Production and Structure Core Facility, School of Life Sciences, EPFL, Lausanne, Switzerland

[#] These authors contributed equally to this work.

Abstract

Many biochemical reactions require controlled recruitment of proteins to membranes. This is largely regulated by post-translational modifications. A frequent one is S-acylation, which consists of the addition of acyl chains and can be reversed by poorly understood acyl protein thioesterases (APTs). Using a panel of computational and experimental approaches, we dissect the mode of action of the major cellular thioesterase APT2 (LYPLA2). We show that soluble APT2 is vulnerable to proteasomal degradation, from which membrane binding protects it. Interaction with membranes requires three consecutive steps: electrostatic attraction, insertion of a hydrophobic loop, and S-acylation by the palmitoyltransferases ZDHHC3 or ZDHHC7. Once bound, APT2 is predicted to deform the lipid bilayer to extract the acyl chain bound to its substrate and capture it in a hydrophobic pocket to allow hydrolysis. This molecular understanding of APT2 paves the way to understand the dynamics of APT2-mediated deacylation of substrates throughout the endomembrane system.

Introduction

Millions of separate reactions occur simultaneously to control every aspect of how a cell functions and behaves. This requires exquisite spatial and temporal control of proteins, often through post-translational modifications. One of the most frequent, affecting 10 to 20% of

[*]Corresponding Authors: F. Gisou van der Goot (gisou.vandergoot@epfl.ch) and Matteo Dal Peraro (matteo.dalperaro@epfl.ch).
[4]Present address: P.A.S.: Department of Applied Physics, Science For Life Laboratory, KTH Royal Institute of Technology, Solna, Sweden;

Author Contributions

Conceptualization, L.A., M. A., P.A.S, M.D.P., G.V.D.G.; Investigation, L.A., M.A., S.H., M.J.M., M.U.A., P.A. S, G. F., F.P.; Funding Acquisition, M.D.P. & G.V.D.G.; Writing–Original Draft M.A., L.A., S. H., M.J.M., M.D.P., G.V.D.G.; Writing–Review & Editing, L.A., M.A., S.H., M.J.M., M.U.A., P.A. S, G. F., F.P., M.D.P., G.V.D.G.; Resources, S.H., L.A.

Competing Financial Interests Statement

The authors declare no competing interests.

Europe PMC Funders Author Manuscripts

the human proteome, is S-acylation [1,2], which can modify a plethora of signaling molecules, such as the EGF receptor or Ras, adhesion molecules, and many transporters. S-acylation is also a key modification in the life cycle of viruses [3] and parasites [4]. This lipidation may affect the trafficking, function, or turnover rate of proteins, and therefore its reversibility is an essential part of its regulatory capacity[5]. Little is known, however, about acyl protein thioesterases (APTs), the proteins responsible for removing the acyl chains [6,7]. Therefore, we herein focused on understanding the mode of action of APT2, a major cytosolic thioesterase, that is involved in the palmitoylation cycle of a variety of proteins, such as the TNF receptor[8], the melanocortin 1 receptor[9], and the palmitoyltransferase ZDHHC6[10].

Similar to other lipid modifications, S-acylation increases the lipophilicity of proteins, thereby affecting their ability to interact with membranes or membrane domains. S-acylation is however unique in being reversible[11–14]. During enzymatic S-acylation, medium chain fatty acids are added to cysteine residues through the action of acyltransferases of the ZDHHC family, which are transmembrane proteins with an active site on the cytosolic side of the membrane. Regulatory removal of the fatty acid is mediated by cytosolic APTs[15,16], wherein all identified members belong to the α/β hydrolase super family. APT2 is a soluble globular enzyme that can undergo S-acylation at its N-terminus on Cys2[17,18], but this should be insufficient to allow stable association with membranes[19] and encounter with its substrate.

The structure of an inhibitor-bound form of APT2 has been solved[20]. How APT2 interacts with the membrane and how it catalyzes the release of the fatty acid attached to its targets is however not known. To investigate these aspects, we first chose a structural approach combining X-ray crystallography and molecular dynamics (MD) simulations. We identified a loop, coined the ß tongue, which mediates membrane interaction both *in vitro* and *in vivo.* This step precedes and is necessary for APT2 S-acylation. We identified the involved palmitoyltransferases and show that acylation is essential for its in vivo function. We identified a hydrophobic pocket within APT2 that can capture the acyl chain, position it in a hydrophobic pocket allowing the thioester bond to be cleaved in the catalytic site. Molecular dynamics simulations further predict that APT2 can deform the lipid leaflet to which it binds, thus contributing to the extraction of the substrate-bound acyl chain from the membrane. Finally, we show that cells tightly control the concentration of soluble APT2 through a mechanism built into the ß tongue, where a sensitive ubiquitination site can be protected in the membrane bound state. Altogether we provide a detailed and previously unknown view of how APT2 mediates de-acylation and is regulated in the cell, helping broaden our picture of how S-acylation cycles control major cellular processes.

Results

APTs are monomers in solution

Our first goal was to perform a crystallization study on full length APTs, as opposed to previous N-terminal truncated versions [21], and to compare WT and mutants. APT1 and APT2 are 68% identical and essentially have the same structure[20,22]. Since as reported[20], APT1 is more stable and thus more amenable to crystallization, we performed our crystallization studies on APT1. We produced full-length wildtype (WT) human APT1,

palmitoylation deficient (C2S) and a catalytically inactive (S119A) mutants. All variants could be successfully crystalized (Supplementary Table 1). As reported [21], APT1 has a near-canonical α/β hydrolase fold with a typical catalytic triad (Fig. 1ab). When compared to the canonical α/β hydrolase fold, APT1 and APT2 have an atypical insertion of four short antiparallel β strands (labeled S1-S4, Fig. 1b), which as described below, are critical to their acylthioesterase function.

Our variants crystallized into different forms, with space group $P4_12_12$ for WT APT1, $P2_12_12$ for C2S APT1, and $P6_4$ for S119A APT1 (Supplementary Table 1). The average RMSD for the 230 common C_α atoms between our APT1 structure and the first published APT1 (PBD id: 1FJ2) [21] was 1.2 Å. The asymmetric units of the crystals however contained 2 or 6 monomers (Supplementary Table 1). For each structure, EPPIC [23] predicted the possible existence of biological dimers. Our WT and C2S X-ray structures showed a similar intermolecular dimeric interface (RMSD ~1.1 Å). In contrast, the previously solved APT1 structure (PBD id: 1FJ2) [21] and the catalytically inactive APT1 mutant (S119A) had largely different dimer conformations (RMSD ~24 Å) (Extended Data Fig. 1a). Principal component analysis on atomistic MD simulations of the WT structure highlighted a large rotational motion centered at the dimer interface (Extended Data Fig. 1b). Therefore, previous and current crystallographic evidence and MD simulations indicate that the dimeric arrangement of APT1 is intrinsically flexible. Interestingly, the dimer interfaces included the APT1 catalytic pocket such that it was partially occluded by the adjacent protomer. Similar observations were made regarding APT2[20]. Backbone RMSD calculations on superimposed APT2 structures in the dimeric conformation (PDB: 6BJE and 5SYN)[20] also showed a large displacement (RMSD ~14 Å, Extended Data Fig. 1cd) again suggesting a flexible dimer interface[20].

We next addressed the stoichiometry of APTs in solution. We measured molecular weights using size-exclusion chromatography (SEC) coupled to multi-angle light scattering (MALS). The mass determined was 29 kDa for APT1 and 32 kDa for APT2 (Fig. 1c), close to the theoretical molecular weights of their monomers (25 and 27 kDa, respectively). These observations reconcile the findings of flexible, heterogeneous dimer interfaces in APT1 and APT2 under crystallization conditions and suggest that the APTs act as monomeric entities in solution and most likely also when interacting with membrane surfaces, as the catalytic site would otherwise be occluded.

Intrinsic membrane binding affinity of APTs

The target proteins of APTs are S-acylated proteins, therefore membrane associated. So, to reach their substrates, APTs must be near membranes. We explored whether APTs can interact with membranes directly using coarse-grained MD simulations in the presence of a palmitoyl-oleoyl-phosphatidylcholine (POPC) bilayer model using the X-ray structures of APT1 (solved in this work) and of APT2 (PDB id 5SYN) as initial models. The simulations showed that APT1 and APT2 invariably end up interacting with the membrane bilayer on a μs timescale (Fig. 1d) and always via the same surface (Fig. 1ef), corresponding to the dimer interface observed in the APT structures (Extended Data Fig. 1). Electrostatic calculations showed that the membrane-interacting surfaces of APT1 and APT2 contained highly

positively charged regions that likely promote the initial association by long-range electrostatic attraction (Fig. 1e). APT1 has two distinct positively charged regions (region A: Arg18, Lys19, His48 and Lys50; region B: His28, His35 and His55) (Fig. 1e, left), while APT2 has a single larger area (His38, His58, Arg61, Lys69, Lys94) (Fig. 1e, right). Interestingly, once close to the membrane, APT1 and APT2 use the S1 and S2 strands and the G1 3_{10} helix, which are mostly hydrophobic, as anchors to the membrane (Fig. 1f). By analogy to a similar membrane-anchoring loop in the pore-forming toxin cytolysin A (ClyA) [24], we coined the S1-G1-S2 loop the ß tongue. S1, S2 and G1 are part of the atypical insertion that APTs have when compared to classical α/β hydrolases (Fig. 1b).

Multistep APT membrane binding

To test the MD prediction that APTs have intrinsic membrane binding activity, we incubated purified APT1 and APT2 with liposomes composed of phosphatidylcholine: phosphatidylserine:phosphatidylethanolamine (PC:PS:PE 2:2:1). The mixtures were subsequently submitted to a sucrose flotation step gradient to separate vesicle-bound from unbound protein. While the proteins remained in the bottom fraction in the absence of liposomes, they were recovered at the top interface when liposomes were present (Fig. 2a), indicating an interaction with the membrane. Analysis of the APT-bound liposomes by electron microscopy confirmed the presence of a layer of proteins decorating the membrane surface (Fig. 2b).

To analyze whether the positive patch at the surface of APTs and the ß-tongue play a role in APT2 membrane binding, we generated mutant proteins anticipated to affect one or the other. We focused mostly on APT2 because, as opposed to APT1 that is most abundant in mitochondria [25], APT2 is found on the cytosolic side of membranes and is thus topologically able to revert the action of ZDHHC enzymes. We produced the quintuple H38A-H58A-R61A-K69A-K94A APT2 mutant, which we coined PosPatch for Positive Patch. To affect the ß tongue, we generated mutants with the rationale of perturbing its electrostatic properties and affect the interplay with the membrane. We produced the M68Q, M68E, M70T, and M68E-M70T APT2 mutants as well as the M65E APT1 mutant. Secondary structure analysis indicated that the PosPatch and the ß tongue mutations did not significantly affect the APT2 secondary structure (Fig. 2c). We also performed unfolding studies measuring the change in ellipticity at 222 nm as a function of temperature. The melting temperature was similar for WT and mutant APT2s (Fig. 2d), indicating that the stability of the proteins was preserved. The PosPatch mutant showed a somewhat steeper unfolding curve, consistent with our observation that this mutant tends to precipitate. Using a colorimetric assay, we verified that the *in vitro* deacylating activity was only moderately affected by the mutations (Fig. 2e and Extended Fig. 1f). Not surprisingly given its reduced stability, the PosPatch mutant was most affected. Finally, we tested the liposome binding capacity. While the M68Q behaved like WT APT2, all other mutants failed to stably bind liposomes (Fig. 2f). Similarly, the M65E APT1 ß tongue mutation impaired liposome binding (Extended Data Fig.1e). Altogether, these experiments confirm the predictions from the MD simulations that APTs have intrinsic membrane binding affinity driven by the positive patch and the ß tongue.

Soluble APT2 mutants are targeted to the proteasome

We next analyzed the expression of the APT2 mutants in cells. The PosPatch mutant was well expressed as witnessed by microscopy and biochemical analysis (Fig. 3ab). Its cellular localization, however, differed markedly from that of the WT protein (Fig. 3a). Instead of showing an accumulation on the Golgi apparatus as reported, it appeared cytosolic. To test the membrane binding capacity of the mutant, we submitted post-nuclear supernatants (PNS) to high speed centrifugation. Analysis of the pellet and the supernatant showed that while WT APT2 was mostly found in the pellet, the PosPatch mutant was more abundant in the supernatant (Fig. 3c). These observations confirm the *in vitro* experiments that the positive patch is necessary for APT2 to bind to membranes.

To our surprise, the ß tongue mutants that failed to bind liposomes were barely expressed upon transient transfection in HeLa cells (Fig. 3d, control). Expression could be rescued by the proteasome inhibitor MG132 (Fig. 3d, +MG132), suggesting that the mutants were synthesized by the cell but rapidly degraded. To confirm this, we performed ^{35}S-Cys/Met metabolic pulse-chase experiments. While the apparent half-life of WT APT2 after a 20 min pulse was approximately 5 h, it dropped to <2 h for the M68E and M70T mutants (Fig. 3e).

Immunofluorescence analysis of the ß-tongue mutants showed a cytosolic-like staining in cells treated for 4 h with MG132, similar to that of the PosPatch mutant (Fig. 3f). The inability to bind to membranes was confirmed biochemically by submitting the PNS to high speed centrifugation. The M68E and M70T mutants were exclusively found in the supernatant (Fig. 3g). This indicates that ß tongue APT2 mutants, which failed to bind to liposomes, remained cytosolic when expressed in cells and underwent rapid proteasome-mediated degradation.

S-acylation mediates stable APT2 membrane association

WT APT2 accumulation on the Golgi apparatus (Extended Data Fig.3a) was reported to depend on Cys2 [7,18] and its likely S-acylation. Using the C2S mutant, we confirmed that palmitoylation occurs on Cys2 (Extended Data Fig.2a) and that the WT protein accumulates on the Golgi in a Cys2-dependent manner (Extended Data Fig.3a). In agreement with the microscopy (Extended Data Fig.3a), the C2S mutant was mostly found in the cytosolic fraction after high speed centrifugation of the PNS (Extended Data Fig.3b).

We next tested whether S-acylation influences APT2 turnover rates using ^{35}S-Cys/Met metabolic pulse-chase experiments. Since APT2 has been proposed to undergo deacylation[17,18], we tested the effects of the general protein deacylation inhibitor Palmostatin B. The C2S mutant had a shorter apparent half-life (≈3 h) than WT APT2 (≈5 h) (Extended Data Fig.3c and Extended Data Fig. 2b). As expected, the decay of C2S was not affected by Palmostatin B treatment. In contrast, degradation of WT APT2 was drastically slowed down by Palmostatin B, the half-life increasing to more than 20 h (Extended Data Fig.3c and Extended Data Fig. 2c). This is not due to an effect of membrane binding on protein stability *per se,* since the melting curve of APT2 was the same in solution and when bound to liposomes (Extended Data Fig. 2d). Instead, the cellular instability likely indicates that cytosolic APT2 is recognized by a quality control mechanism.

The S-acylation of APT2 is thus required for stable membrane association, and this modification drastically affects APT2 turnover rates. The strongly stabilizing effect of Palmostatin B also suggests that APT2 undergoes significant depalmitoylation in cells, consistent with previous observations[17].

Three-step mechanism of APT2 membrane association

We next investigated the steady state S-acylation status of APT2 in cells by performing a capture assay for S-acylated proteins termed Acyl-RAC. We analyzed both the cytosolic and pellet fractions of the PNS. Acylated WT APT2 was readily detectable in the pellet fraction, but not in the supernatant (Extended Data Fig.3d), indicating that cytosolic APT2 is not S-acylated.

Given that the ß tongue mutants were also found in the soluble fraction, this suggests that despite the presence of the cysteine at position 2, these mutants might not undergo S-acylation. To test this, ß tongue mutants were expressed in HeLa cells and their degradation was prevented by MG132 treatment. The incorporation of ^{3}H-palmitate was monitored. While palmitoylation of WT APT2 was readily observed, the membrane-binding-deficient ß tongue mutants did not undergo detectable palmitoylation (Extended Data Fig.3e).

Our observations altogether indicate that APT2 undergoes a three-step membrane-binding process in the cell: (i) electrostatic interactions bring APT2 to the membrane, where (ii) the ß tongue dips into the membrane to hold APT2 temporarily in place. This is necessary for APT2 to encounter its S-acylating enzyme(s), (iii) leading to the lipidation of Cys2 and a stable membrane association. The effect of Palmostatin B on APT2 stability further indicates that APT2 can undergo deacylation and membrane release.

ZDHHC3 and 7 mediated APT2 S-acylation

We next analyzed whether S-acylation is important for APT2 to modify its targets *in vivo*, as APT2 is a soluble enzyme and its targets are membrane bound. As a readout for *in vivo* activity, we monitored the APT2-dependent depalmitoylation of one of its targets, the zDHHC6 protein[10]. Expression of endogenous APT2 was silenced (Extended Data Fig. 2e) and cells were subsequently recomplemented with either WT or C2S APT2. The cells were pulsed for 2 h with ^{3}H-palmitate and chased for 0 or 3 h to allow APT2-mediated depalmitoylation. zDHHC6 was then immunoprecipitated, and its palmitoylation level was monitored by autoradiography[10]. Upon expression of WT APT2, depalmitoylation of ZDHHC6 was observed at 3 h (Fig. 4a). However, C2S APT2 failed to mediate ZDHHC6 depalmitoylation (Fig. 4a), consistent with our previous overexpression studies[10]. These observations indicate that the S-acylation site at position 2 is necessary for APT2 to deacylate ZDHHC6. From our *in vitro* assays on purified, non-acylated, APT2, we know that S-acylation is not required for the acyl thioesterase activity per se, as reported (Pedro *et al*, 2013). These observations therefore indicate that in the cellular context, APT2 requires S-acylation to be able to modify at least a subset of its targets.

Given the importance of S-acylation on APT2 localization, cellular stability, and *in vivo* activity, we performed a screen to identify the involved ZDHHC enzyme(s). Because APT2 accumulates on the Golgi when acylated, we could screen by fluorescence microscopy. We

first silenced ZDHHC enzymes by dividing them into 6 pools. The efficiency of the siRNAs was previously reported[10]. Silencing pool M1, containing siRNAs against ZDHHC 1, 3, 7, 13, and 17, led to the Golgi release of APT2 (Extended Data Fig. 4a). We subsequently silenced each ZDHHC enzyme individually and found that none of them led to complete release of APT2 from the Golgi. We therefore silenced them in pairs. Simultaneous silencing of ZDHHC3 and 7 (Fig. 4bc, Extended Data Fig. 4a), but not of 13 and 17 (Extended Data Fig. 4a), led to APT2 release from the Golgi. ZDHHC3- and 7-dependent palmitoylation of APT2 was confirmed by ^{3}H-palmitate incorporation (Fig. 4d). ZDHHC3 and 7 are phylogenetically related [26], but differ in terms of localization, with ZDHHC3 mainly present in the Golgi, while we found ZDHHC7 predominantly in the ER (Extended Data Fig. 4bc), although Golgi localization has been reported [27,28].

Future studies will address the trafficking routes of APT2 through the cell. The existence of an ER ZDHHC enzyme already indicates that APT2 should stably interact with the ER. Upon silencing of ZDHHC3, leaving ZDHHC7 as the only enzyme acting on APT2, Golgi accumulation was still visible. This could be explained by S-acylated APT2 moving by vesicular trafficking from the ER to the Golgi. The absence of a clear APT2 ER staining indicates that this export route out of the ER must be relatively rapid, when compared to transport of APT2 out of, or release from, the Golgi, hence the Golgi accumulation. APT2 must however be present on the ER within the apparently “cytosolic” staining of our microscopy images. With the aim of capturing this ER-associated APT2 pool, we performed Fluorescence Recovery After Photobleaching (FRAP) experiments. The reasoning was that a proportion of the apparently cytosolic WT APT2 should, if membrane bound, have a reduced mobility and therefore a slower fluorescence recovery time after photobleaching, as compared to a soluble protein. We performed FRAP experiments on WT APT2, C2S APT2, and on mCitrine and mCherry-mCitrine as two soluble cytosolic protein controls. Bleaching was performed outside of the Golgi area. The fluorescence recovery time was similar for mCitrine and mCherry-mCitrine (Extended Data Fig. 4d). It was shorter for mCitrine than for C2S APT2, consistent with the ability of C2S to transiently interact with membranes through its ß tongue (Fig. 4ef). The longest recovery time was determined for WT (Fig. 4ef), indicating that something is reducing its mobility, which depends on Cys-2, thus consistent with S-acylation on this site playing a role. These observations suggest that WT APT2 interacts with cellular membranes other than that of the Golgi.

Control of APT2 turnover by the ß tongue

APT2 interaction with membranes appears to protect it from proteasomal degradation. To understand this mechanism, we searched for lysine residues that could be ubiquitination targets. APT2 contains 6 lysines, one of which appears ideally positioned at the very tip of the ß tongue, Lys-69 (Fig. 5a). We generated K69R variants of WT and the ß tongue mutants. Remarkably, the K69R mutation led to full rescue of ß tongue mutant expression and loss of the ubiquitination signal (Fig. 5b). Introducing the K69R mutation also led to an increase in C2S expression (Fig. 5b). These observations reveal that APT2 has a built-in mechanism whereby soluble APT2, through the exposure of Lys-69, can be ubiquitinated and targeted to degradation, while membrane-bound APT2 dips Lys69 in the membrane, hiding it from the ubiquitin ligase.

Rescuing the expression of the ß tongue mutants by the K69R mutation was however insufficient to confer *in vivo* deacylating activity, as monitored by measuring the APT2-dependent depalmitoylation of ZDHHC6 (Fig. 5cd). These observations confirm that in cells the ability of APT2 to deacylate target proteins requires both the ß tongue and acylation of Cys2.

Identification of a palmitate binding pocket in APTs

To further understand how APTs act on their substrates, we reanalyzed our APT1 crystal structures. We noticed that about one third of the proteins in the asymmetric unit contained a fatty acid in a hydrophobic pocket in the vicinity of the catalytic site (Fig. 6a, Extended Data Fig.5a). The electron-density maps specifically identified a palmitic acid, with the carboxylate group facing the catalytic Ser119. The ligand could be extracted with ethanol and analysed by ultraperformance liquid chromatography quadrupole-time-of-flight mass spectrometry, confirming the presence of the palmitic acid in all three structures (WT, C2S, and S119A APT1) (Fig. 6b). The fatty acid was not added at any step and must have been retained during purification, as observed for other proteins[29].

Thioesterases have been reported to be inhibited by 2-bromopalmitate (2-BP), a widely used palmitoylation inhibitor[30]. 2-BP inhibited APT2 *in vitro*, as efficiently as its specific inhibitor ML349 (Extended Data Fig.5b) and *in vivo* (Extended Data Fig.5cd). 2-BP also inhibited APT1, but with a lower affinity (Extended Data Fig.5b). Nonetheless, crystallization of APT1 in the presence 2-BP led to the presence of palmitate in all proteins of the unit cell (Extended Data Fig. 5e).

The aliphatic chain of the palmitic acid was sequestered in a largely non-polar cavity of APT1. A solvent accessible entrance is located close to the loop between helices S3-S4 (Extended Data Fig.5f, Leu78, Ser79, and Pro80). The pocket is surrounded by residues from helix E (Phe181 and Leu184), by Leu30, Ile75, Ile76, and Leu176 and capped by Cys144, Trp145, Leu146, and Pro147 (Extended Data Fig.5f). In the apo form, the pocket was somewhat closed, due to movement of the S3-S4 loop and the adjacent E helix (Extended Data Fig.5g). The volume changed from 124 $Å^3$ in the apo enzyme to 226 $Å^3$ in the ligand bound form, through rearrangements of Leu78, Phe181, and Leu184.

Palmitate was modeled into the corresponding pocket of APT2 (Fig. 6c),PDB id 5SYN). Since residues Trp148, Phe183, Leu186, and Thr187 are part of the hydrophobic cavity, recombinant variants were produced (F183R, F183E, and L186K) and their deacylation activity tested *in vitro*. Mutating Phe183 abolished the acylthioesterase activity, while mutating Leu186 had no effect (Fig. 6d). For *in vivo* activity testing, we probed a larger panel of mutants. All six mutants were well expressed (Extended Data Fig. 6a and underwent S-palmitoylation (Extended Data Fig. 6b). However, with the exception of the W184Q mutant, all hydrophobic pocket mutants (F183E, F183R, W148R, L186R, T187R) failed to depalmitoylate ZDHHC6 (Extended Data Fig. 6c, showing that the hydrophobic pocket of APT2 is essential for its protein acylthioesterase activity.

Altogether, these observations indicate that the acyl chain of a palmitoylated substrate protein needs to access this newly discovered APT hydrophobic pocket for hydrolysis to

occur. This means that the acyl chain must first be extracted from the membrane containing the APT2-target protein. We wondered whether APT2 may affect the membrane's structure in a manner that would favor movement of the acyl chain out of the bilayer into the pocket. To evaluate this possibility, we monitored the thickness of the lipid bilayer upon interaction of APT2 with the membrane during MD trajectories (Fig. 6e). We observed that while the average membrane thickness was ~40 Å in the absence of APT2, when APT2 was bound, the thickness increased to ~47 Å (Fig. 6f, Extended Data Fig. 6d). The protein perturbed mostly the upper leaflet of the bilayer by increasing its thickness locally from 17 Å to 25 Å (Fig. 6f). Although simulations at this level of theory cannot explore the complete deacylation reaction mechanism, the local membrane deformation promoted by APT2 could favor the extraction of palmitate covalently linked to the substrate.

Discussion

Though acyl protein thioesterases are critical components of acylation-deacylation-regulated protein localization and function [2,5], little is known about how they act in cells and how they are controlled. Combining a panel of approaches, we herein studied the mode of action of the thioesterase APT2. We discovered how APT2 approaches membranes to stably associate with them, how it extracts the acyl chain that is to be removed from its targets, and how cells regulate the cellular amounts of APT2 through two counteracting post-translational modifications, S-acylation and ubiquitination.

We could determine that the stable binding of APT2 to cellular membranes requires three steps: (i) long range electrostatic interactions mediated by patches of positively charged residues that allow APT2 to approach membranes and (ii) to dip in its ß tongue, and (iii) S-acylation of Cys2 by the acyltransferases ZDHHC3 or 7. This last step is required for APT2 to modify at least a subset of its targets in the cellular context. This is presumably because APT2 needs to have a sufficient dwell time on membranes to encounter its membrane-associated S-acylated target proteins. The localization of ZDHHC3 and ZDHHC7, respectively present on the Golgi and the ER, will also influence the ability of APT2 to encounter its targets. The complete understanding of APT2 trafficking in cells awaits further investigation.

The crystallization studies revealed a hydrophobic pocket in APT2 that is essential for the enzyme's activity. This finding indicates that the target-bound acyl chain must transfer from the membrane to the hydrophobic pocket of APT2 to position the thioester bond between the acyl chain and the target protein at the catalytic site. Analysis of the MD simulations indicated that beneath the catalytic pocket, APT2 may trigger a membrane deformation, pulling up the lipid monolayer. Future studies need to address this experimentally.

APT2 has an interesting built-in mechanism that targets it to degradation when free in the cytosol. This is mediated by a ubiquitination site (Lys69) within the ß tongue, which is inaccessible when the protein is membrane bound. Why excess APT2 is deleterious to the cell remains to be understood. The level of cytosolic APT2 may differ between cell types, since in CHO and astroglial cells, a large fraction of APT2 was found to be cytosolic[17,30].

The relative abundance of APT2 in the cytosol and on membranes, in particular de Golgi, may therefore vary between cell types as a function of ZDHHC3 and 7 expression.

We propose the following mode of action: soluble APT2 weakly interacts with cellular membranes via its ß tongue; in this state, it can detach from the membrane or encounter ZDHHC3 or 7, which can add an acyl chain to Cys2, allowing APT2 to stably bind and explore the membrane in search of potential substrates. Upon encounter with a substrate, APT2 triggers extraction of the acyl chain from the membrane allowing it to move into the APT2 hydrophobic pocket. With this ideal positioning, hydrolysis may occur. Membrane bound APT2 can itself undergo deacylation and subsequent release from the membrane. The cycle can then repeat itself on the same or a different membrane compartment. In its cytosolic form, however, APT2 is vulnerable to ubiquitination, which targets it to the proteasome for degradation.

Overall, these studies on APT2 have shown us how a key regulator of S-acylation functions and is controlled. With this information, we can now start addressing the dynamics and spatio-temporal regulation that allow a single enzyme, APT2, to modify many targets proteins that localize to different compartments of the endomembrane system, including the plasma membrane[7,31–33] and the ER[10].

Methods

Cell lines

HeLa cells (ATCC) were grown in complete modified Eagle's medium (MEM, Sigma) at 37°C, supplemented with 10% fetal bovine serum (FBS), 2 mM L-Glutamine, penicillin, and streptomycin.

Plasmids and transfection

Human influenza hemagglutinin (HA), Myc or Citrine fusions of APT1 or APT2 were inserted into pcDNA3.1-N1. All mutations of APT1 and APT2 were generated using QuikChange mutagenesis kit (Stratagene). The Myc fusion of ZDHHC6 was cloned in pcDNA3.1. For the control transfection, we used empty pcDNA3.1 plasmid. Plasmids were transfected into HeLa cells for 24 h (2 μg of cDNA/9.6 cm^2 plate) using Fugene (Promega). For gene silencing, HeLa cells were transfected for 72 h with 100 pmol/9.2 cm^2 dish of siRNA using Interferin (Polyplus) transfection reagent. For the control siRNA, we used the following target sequence from the viral glycoprotein VSV-G: 5'-ATTGAACAAACGAAACAAGGA-3'. For human APT2 siRNA, we used the following sequence to target the 3' non-coding region: 5'-CAGCTGCTTCTCAGTCATGAA-3'. siRNAs against all human ZDHHC genes were the same as previously published [34].

Antibodies and drugs

The following primary antibodies were used: mouse anti-Calnexin (Millipore, MAB3126, RRID: AB_2069152), mouse anti-Tubulin (Sigma, T5168, RRID: AB_477579), mouse anti-Actin (Millipore,MAB1501, RRID: AB_2223041), rat anti-HA-HRP (Roche, 12013819001, RRID: AB_390917), mouse anti-Myc (SIGMA, 9E10 M4439, RRID: AB_439694), mouse

anti-Ubiquitin (Enzo, P4D1, PW0930, RRID: AB_1181462), rat anti-HA (Roche, 3F10, RRID: AB_390918), rabbit anti-Giantin (Abcam, ab24586, RRID: AB_448163), anti-GM130 (BD, clone35, RRID_398141), anti-FLAG (Sigma, M2, RRID_259529). The anti-HA affinity gel (Roche, 1815016001, RRID: AB_390914) or anti-MYC affinity agarose (Pierce, PIER20169) were used for immunoprecipitation.

Drugs were used as follows: MG132 at 10 μM (Sigma, C2211), 4 h at 37°C; Palmostatin B at 1 μM (Calbiochem, 178501), indicated time at 37°C; 2-Bromopalmitate at 100 μM (2-BP; Focus Biomolecules, FBM-10-3284), indicated time at 37°C.

Expression and purification of human acyl protein thioesterases (APT) 1 and 2

Human APT1 and APT2 wildtype and mutant proteins were expressed and purified as described elsewhere [21] with minor modifications. Briefly, BL21 [DE3] (Novagen 70235-3) harboring the appropriate plasmids were grown at 37°C to OD_{600} = 0.6. Protein expression was induced by the addition of IPTG to 0.8 mM and cultures were grown for an additional 18 h at 16°C. Cells were lysed by sonication in ice-cold H Buffer (50 mM Tris-HCl pH 8.0, 150 mM NaCl), and cellular debris was pelleted by centrifugation at 15,000 × *g* for 30 min at 4°C. The supernatant was loaded on a HisTrap HP (GE LifeSciences 17524802), and protein was eluted in H Buffer containing 250 mM imidazole. Where applicable, the N-terminal His6-tag was removed by the addition of His6-rTEV protease (Life Technologies) and dialyzed in H Buffer for 36 h at 4°C. Cleaved protein was harvested, and DTT and EDTA were added to concentrations of 5 mM and 1 mM, respectively.

Circular dichroism (CD) spectroscopy

Circular dichroism (CD) spectra of APT2 were collected using a Chirascan V100 (Applied Biophysics) and 1 mm pathlength quartz cuvettes (Hellma 110-QS). Spectra were collected in triplicate at 1 nm intervals between 280 and 207 nm. The temperature of the 6-cuvette holder was monitored and controlled by a Quantum Northwestern CD 250 Peltier system. For denaturation curves, the temperature of the sample was increased from 4°C to 94°C by 2°C intervals; spectra were collected at each temperature following a 30 s equilibration period.

Thioesterase Activity Assay

The thioesterase activity assay was modified from Kemp et al. [35]. Recombinant APT was preincubated for 10 min at room temperature with either DMSO or inhibitor in DMSO, where applicable. The reaction was initiated by the addition of 4-methylumbelliferyl palmitate (Santa Cruz Biotechnology sc-214256, PubChem CID 87248) and Pluoronic® F-127 (ThermoFisher P3000MP, PubChem CID24751). Enzyme activity was monitored by the appearance of methylumbelliferone over time (Ex 360 nm, Em 449 nm). The assay was optimized to use 0.4 μM of enzyme, 0.1 mM of substrate, and 0.1% detergent in HBuffer for a 96-well plate format. The following compounds were used as inhibitors: ML348 (TOCRIS 5345, PubChem CID 3238952), ML349 (TOCRIS 5344, PubChem CID 16193817), and 2-Bromopalmitate (Fisher Scientific AC218610500, PubChem CID 82145).

Crystallization and structure determination

Crystals of APT1 WT, S119A, and C2S bound or not to 2-Bromopalmitate were grown by sitting drop vapor diffusion at 18°C from a 1:1 mixture of protein solution (at ~10 mg/ml in H Buffer with 5 mM of DTT and 1 mM of EDTA) and reservoir solution. For the 2-BP complex crystals, the protein at 10 mg/ml was incubated with 2-BP at a final concentration of 5 mM for 10 min at room temperature before setting up the crystallization drops. The respective reservoir solutions contained: 10% w/v of polyethylene glycol (PEG) 8000, 10% w/v PEG 1000, 0.2 M potassium bromide, 01.M sodium acetate at pH 5.5 for WT; 25% of PEG 2000 MME (monomethyl ether), 0.3 M sodium acetate, 0.1 M sodium cacodylate pH 6.5 for C2S and S119A; and 0.1 M imidazole, 0.1 M MES (2-(N-morpholino)ethanesulfonic acid) monohydrate, 20% v/v PEG 500 MME, 10% w/v PEG 2000, 20 mM 1,6-hexanediol, 20 mM 1-butanol, 20 mM 1,2-propanediol, 20 mM 2-propanol, 20 mM 1,4-butanediol, 20 mM 1,3-propanediol, pH 6.5, for C2S bound to 2-BP. Crystal growth occurred over a period of 5 to 15 days.

Crystals were flash frozen by immersion in liquid nitrogen after soaking in cryoprotectant solution (reservoir solution supplemented with 25% w/v glycerol). X-ray diffraction data were collected on beamline X06DA at the Swiss Light Source (SLS, PSI, Villigen Switzerland) at -173.15°C (100 K). The X-ray wavelengths used were 0.826 Å for WT, 1 Å for C2S and S119A, and 0.919 Å for C2S/2-BP. Data were indexed, integrated, and scaled with XDS [36]. Phase determination was carried out by molecular replacement using Phaser (McCoy *et al*, 2007) of CCP4 Suite and the published structure of hAPT1 (PDB: 1FJ2) as a template. Coot [37] was used for graphical map inspection and manual rebuilding of atomic models. Phenix [38] was used for structure refinement. The WT crystals contained 6 molecules in the asymmetric unit (AU), while the C2S and S119 mutants pack with 4 and 2 molecules in the AU, respectively. Apo-crystals contained residual palmitic acid molecules originating from *E. coli* in 50% of the molecules in the AU. However, there is full occupancy of the 2-BP in the C2S/2-BP complex crystals. The occupancy of 2-BP was confirmed by Br-anomalous difference maps, as the crystals were radiated with X-rays of the Br-peak energy. Residues T8/P9 to I229/D230 were modelled in all chains except for chain B in the WT crystals, where residues from N5 could be also modeled. There are no Ramachandran outliers. Crystallographic statistics are listed in Supplementary Table 1. Coordinates and structure factors were deposited in the Protein Data Bank (PDB accession codes: 6QGS for wt/hAPT1; 6QGQ for C2S/hAPT1; 6QGO for S119A/hAPT1; and 6QGN for the C2S-2-BP complex crystals).

Atomistic molecular dynamics simulations

The initial APT1 conformation of the full-length APT1 WT was taken from our crystallographic structures. The resulting model was fully solvated with TIP3P water models[39] in a water box of dimension 70×70×70 $Å^3$ and neutralized by the addition of NaCl at a concentration of 150 mM. The CHARMM36 force field[39] was used for the parametrization of the protein (with CMAP correction). MD simulations were performed with NAMD 2.9 software [40]. The system was minimized for 1000 steps and equilibrated in the NPT ensemble for 5 ns at 1 atm and 300 K using a time-step of 2 fs. The pCys2/APT1 system was then simulated for 0.3 μs in the NPT ensemble. Snapshots were taken at 0.1 ns

time intervals for structural analysis. The system was equilibrated following the protocol reported by Bovigny et al.[40]and was simulated for 0.3 μs in the NPT ensemble. In both simulated systems, the periodic electrostatic interactions were computed using particle Mesh Ewald (PME) summation with grid spacing smaller than 1 Å[41].

Coarse-grained molecular dynamics simulations

The atomistic structure pCys2/APT1 and APT1 were coarse grained from our X-ray structures using the Martini force field [42] and were initially positioned 60 Å from the membrane using the Insane script [42], which generates the POPC phosphatidylcholine bilayer and solvent. The pCys parameters were retrieved from a previous CG study[43]. Five independent replicas, where the protein was aligned with different initial conditions with respect to the membrane, were set up and the resulting systems were minimized and equilibrated for 10 ps in NVT using a timestep of 2 fs. Afterwards, 100 ps of NPT MD with a time step of 20 fs was applied for increasing the temperature and pressure to the range of 300 K and 1 bar, respectively. The temperature was controlled using the Bussi thermostat with a coupling time of 1 ps[44], while the pressure was controlled by a weak semi-isotropic coupling with a reference pressure of 1 bar and a compressibility of 3×10^{-4} bar^{-1}. Production MD trajectories were collected for 4 μs using a time step of 20 fs. All simulations were performed using GROMACS 5.1.2[43].

Analysis of fatty-acid binding

Bound ligands were extracted from APT1 WT by the addition of 500 μL of ice-cold HPLC grade ethanol to 100 μL of protein (at 414 μM). The solution was incubated at -20°C for 3 days and was subsequently centrifuged (16,000 x *g* at 4°C) and evaporated under vacuum. The residual material was resuspended in 200 μL of propanol. Chromatographic separations employed an Agilent Zorbax Extended C18 (2.1 mm x 50 mm, 1.8 μm particle size) reversed-phase column run at a flow rate of 0.4 mL/min. A linear gradient was applied with initial and final mobile phase consisting of 50% water:50% acetonitrile and 100% acetonitrile, respectively. The presence of fatty acid was determined by quadrupole-time-of-flight mass spectrometry (Q-TOF-MS) analyses and comparison with a stock solution (Sigma-Aldrich) composed of four different fatty-acid standards (lauric acid [12:0], myristic acid [14:0], palmitic acid [16:0], and stearic acid [18:0]).

Size-exclusion chromatography with multi-angle laser light scattering

The mass measurements were performed on a Dionex UltiMate3000 HPLC system coupled with a 3-angle miniDAWN TREOS static light scattering detector (Wyatt Technology). Sample volumes of 100 μL of APT1 WT and ATP2 WT at 40 μM were injected into a Superdex 75 10/300 GL column (GE Healthcare) previously equilibrated with 50 mM Tris-HCl pH 8.0, 150 mM NaCl, and 2 mM TCEP at a flow rate of 0.5 mL/min. The data were further analyzed using ASTRA 6.1 software using the absorbance at 280 nm and the theoretical extinction coefficient for concentration measurements.

Liposome floatation assays

Liposomes composed of L-alpha-phosphatidylcholine (Avanti polar lipids 131 601C), L-alpha-phosphatidylserine (Avanti polar lipids 840032C), and L-alpha-phosphatidylethanolamine (Avanti polar lipids 840026C) were prepared in a 2:2:1 molar ratio. Next, 2 μM of phospholipid mix was suspended in 2 mL of HBS pH 7.4. Then, 50 μg of purified protein were incubated with 200 μL of liposomes or with 200 μL of HBS pH 7.4 (control) for 2 h at 10°C. The protein-lipid suspension was adjusted to 40% sucrose and loaded on the bottom of a sucrose step gradient (40%/30%/10% sucrose). After 1 h of centrifugation at 100 000 × *g*, the interfaces were collected from the top (1: between 10 and 30%; 2: between 30 and 40%; and 3: bottom), and 10 μl of each interface were analyzed by SDS-PAGE and Coomassie blue.

^{3}H-palmitic acid radiolabeling experiments

HeLa cells were transfected or not with different constructs, incubated for 3 h in Glasgow minimal essential medium (IM; buffered with 10 mM HEPES, pH 7.4) with 200 μCi/mL of ^{3}H palmitic acid (9,10-^{3}H[N]) (American Radiolabeled Chemicals, Inc.). The cells were washed, and incubated in DMEM complete medium for the indicated time of chase or directly lysed for immunoprecipitation with the indicated antibodies.

For immunoprecipitation, cells were washed three times with PBS, lysed 30 min at 4°C in buffer (0.5% Nonidet P-40, 500 mM Tris pH 7.4, 20 mM EDTA, 10 mM NaF, 2 mM benzamidine and protease inhibitor cocktail [Roche]), and centrifuged 3 min at 5000 rpm. Supernatants were precleared with G Sepharose beads prior to the immunoprecipitation reaction. Supernatants were incubated overnight with the appropriate antibodies and G Sepharose beads. After immunoprecipitation, washed beads were incubated for 5 min at 90°C in reducing sample buffer prior to 4–20% gradient SDS-PAGE. Gels were incubated 30 min in a fixative solution (25% isopropanol, 65% H2O, 10% acetic acid), followed by a 30 min incubation in signal enhancer Amplify NAMP100 (GE Healthcare). The radiolabeled products were imaged using a Typhoon phosphoimager and quantified using Typhoon Imager (ImageQuanTool, GE Healthcare). The images shown for ^{3}H-palmitate labeling were obtained using fluorography on film.

^{35}S-cysteine-methionine radiolabeling experiments

HeLa cells were transfected with different Myc-APT2 constructs for 24 h, the cells were starved in DMEM HG devoid of Cys/Met for 30 min at 37°C, pulsed with the same medium supplemented with 140 μCi of ^{35}S Cys/Met (American Radiolabeled Chemicals, Inc.) for 20 min, washed, and incubated in DMEM complete medium for the indicated time of chase before immunoprecipitation as for ^{3}H-palmitic acid radiolabeling experiments.

Membrane-cytosol separation

To prepare the post-nuclear supernatant (PNS), HeLa cells were harvested, washed with PBS, and homogenized by passage through a 22 G injection needle in HB (2.9 mM imidazole and 250 mM sucrose, pH 7.4) containing a mini tablet protease inhibitor cocktail (Roche). After centrifugation, the supernatant was collected as HeLa PNS.

PNS was centrifuged for 1 h at 100,000 × *g* in a safe-lock Eppendorf tube in a Sorvall MX150 ultracentrifuge. The pellet and supernatant were dissolved in an equal volume of reducing sample buffer and incubated for 5 min at 90°C prior to separation on a 4–20% gradient SDS-PAGE gel.

Acyl-RAC capture assay

Protein S-palmitoylation was assessed by the Acyl-RAC assay as previously described [44] with some modifications. HeLa PNS were lysed in buffer (0.5% Triton-X100, 25 mM HEPES, 25 mM NaCl, 1 mM EDTA, pH 7.4, and protease inhibitor cocktail). Then, 200 µL of blocking buffer (100 mM HEPES, 1 mM EDTA, 87.5 mM SDS, and 1.5% [v/v] methyl methanethiosulfonate [MMTS]) was added to the cell lysate and incubated for 4 h at 40°C to block the free SH groups with MMTS. Proteins were acetone precipitated and resuspended in buffer (100 mM HEPES, 1 mM EDTA, 35 mM SDS). For treatment with hydroxylamine (HA) and capture by Thiopropyl Sepharose® beads, 2 M of hydroxylamine was added together with the beads (previously activated for 15 min with water) to a final concentration of 0.5 M of hydroxylamine and 10% (w/v) beads. As a negative control, 2 M Tris was used instead of hydroxylamine. These samples were then incubated overnight at room temperature on a rotating wheel. After washes, the proteins were eluted from the beads by incubation in 40 µL SDS sample buffer with ß mercaptoethanol for 5 min at 95°C. Finally, samples were separated by SDS-PAGE and analyzed by immunoblotting. A fraction of the PNS was saved as the input.

Immunofluorescence microscopy

Cells were fixed in 4% paraformaldehyde (15 min), quenched with 50 mM NH_4Cl (30 min) and permeabilized with 0.1% Triton X-100 (5 min). Antibodies were diluted in PBS containing 1% BSA. Coverslips were incubated for 1 h with primary antibodies, washed three times in PBS, and incubated 45 min with secondary antibodies. Coverslips were mounted onto microscope slides with ProLong™ Gold Antifade Mountant (P36930; Invitrogen). Images were collected using a confocal laser-scanning microscope (Zeiss LSM 700) and processed using Fiji™ software.

Fluorescence recovery after photobleaching

Experiments were performed on cells expressing mCitrine, APT2-mCitrine or APT2 C2S-mCitrine. Briefly, cells were seeded in 35-mm glass bottom plates (FD35-100, FluoroDish™) and transfected with 2 µg of plasmid DNA using Mirus Transfection Reagent (TransIT-X2, MirusBio). After 24 h of transfection, FRAP experiments were performed on Zeiss LSM700 Invert microscope (Carl-Zeiss AG) with 63X oil-immersion objective. Cells were maintained under normal cell-culture conditions by using a stage top incubator (H301-Mini, Okolab). The images were acquired at 488 nm. A circular region of interest (ROI) of 5 µm radius was bleached with 5 iterations at maximum intensities of both the 405 nm and 488 nm fixed lasers. Fluorescence recovery was then followed for 20 s at 180 ms intervals. Acquisitions were processed using Fiji™ software [45]. After subtracting the background signal, the fluorescence intensities of ROI were divided by the fluorescence intensities of a neighboring unbleached region at each time point, to correct for fluorescence decay over time (Lin *et al*, 2015). The corrected values were analyzed using GraphPad Prism 8.2.1.

Data were fit using non-linear regression and half-time of the recovery was calculated using one-phase association model.

Extended Data

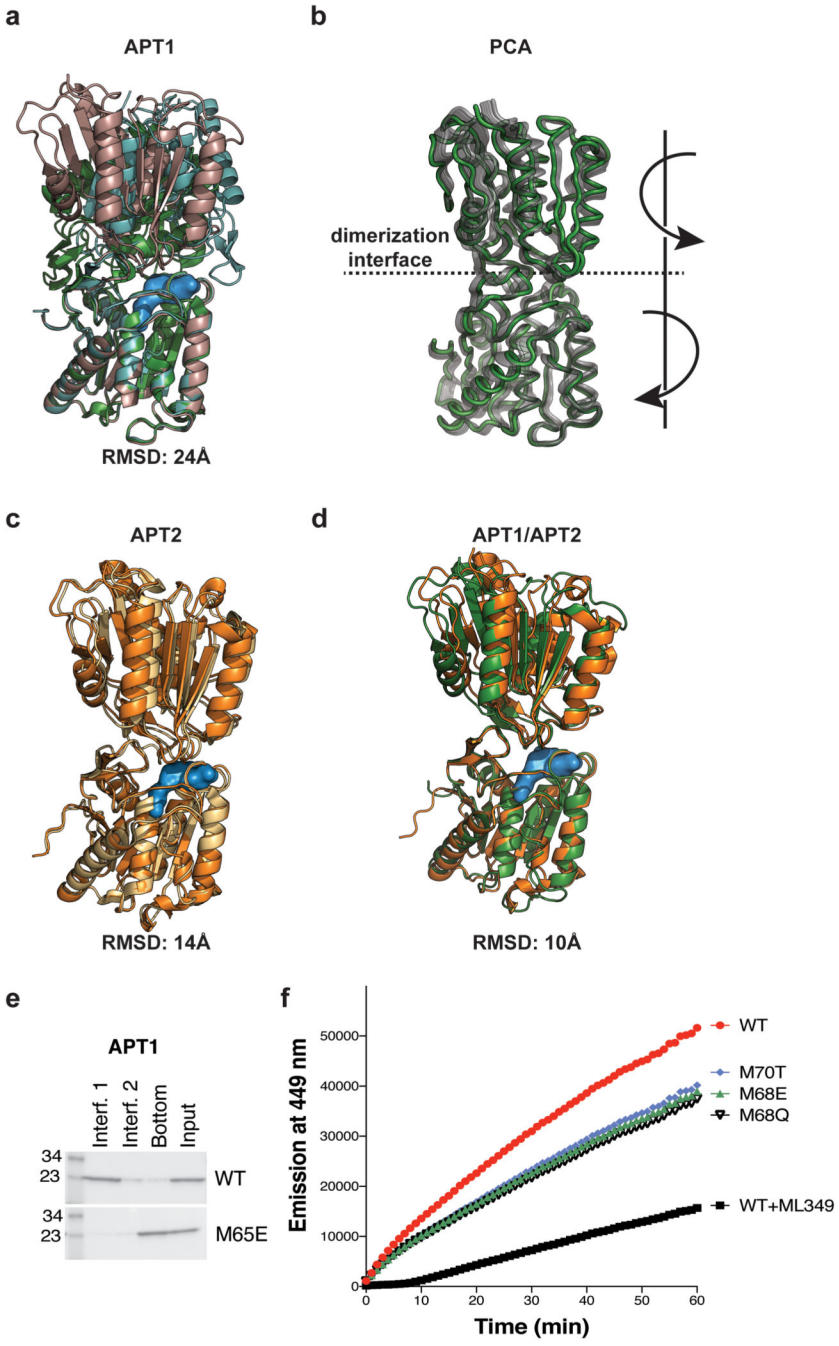

Extended Data Figure 1. The APT crystallographic dimers.

a. Comparative superimposition of S119A APT1/6QGO (light-blue), WT APT1/6QGS (green) and WT APT1/1FJ2 (dark-pink). The average backbone RMSD value is 24 Å. **b.** Principal component analysis based on atomistic MD simulations on the WT APT1; **c.**

Europe PMC Funders Author Manuscripts

Comparative superimposition of WT APT2/5SYN (orange) and WT APT2/6BJE (light yellow). The average backbone RMSD value is 14 Å; **d.** Superimposition of WT APT1/6QGS (green) and WT APT2/5SYN (Orange). The average backbone RMSD value is 20 Å. In surface blue representation are the catalytic residues: S119, D74 and H208. **e**. Association of WT APT1 and β-tongue mutant with liposomes. WT and mutant APT1 proteins were incubated with liposomes and loaded on the bottom of a sucrose gradient. The different interfaces from the top (1) to bottom were collected, loaded on an SDS-PAGE gel, and revealed with Coomassie blue. **f**. The thioesterase activity of WT APT2, the PosPatch or the ß tongue mutants was monitored as a function of time after the addition of substrate and detergent. APT2-specific inhibitor ML349 was included as a positive control. Technical replicates were averaged within each experiment. Average of the activity between multiple independent experiments at time 60 min are shown in Fig. 2.

Europe PMC Funders Author Manuscripts

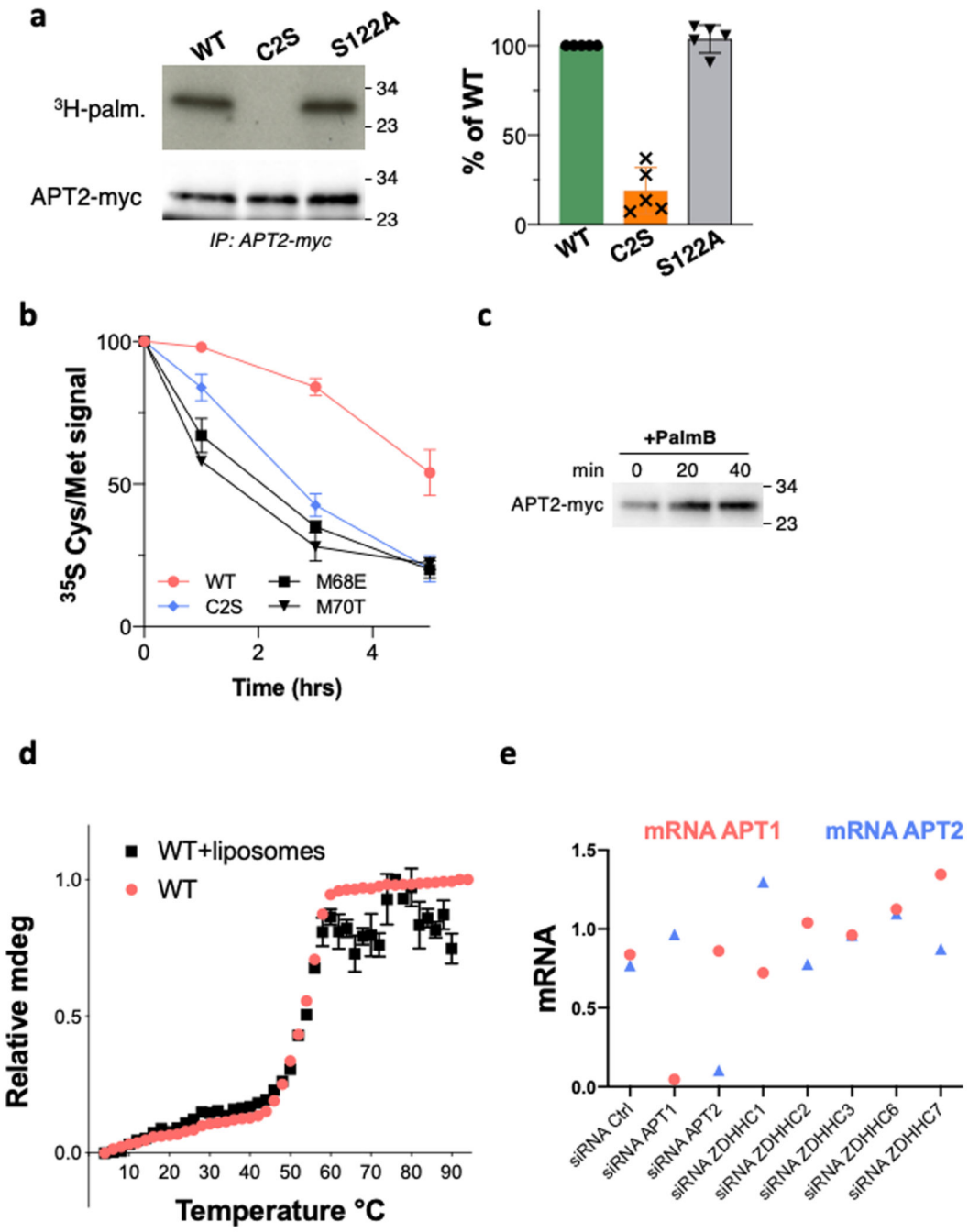

Extended Data Figure 2. WT and palmitoylation deficient APT2.

HeLa cells were transfected with different myc-tagged APT2 constructs for 24 h. **a**. Cells were then metabolically labeled for 3 h at 37°C with ^{3}H-palmitic acid. Proteins were extracted, immunoprecipitated with anti-myc antibodies, subjected to SDS-PAGE gel, analyzed by autoradiography (^{3}H-palm), and quantified using the Typhoon Imager or by immunoblotting with anti-myc antibodies. The calculated value of ^{3}H-palmitic acid incorporation into WT APT2 was set to 100%, and the values for the mutants were expressed relative to this (results are mean SD, n = 5 independent experiments). **b**. Cells

Europe PMC Funders Author Manuscripts

were pulsed with ^{35}S Cys/Met for 20 min and were chased for the indicated time before immunoprecipitation and SDS-PAGE. Degradation kinetics were analyzed by autoradiography, and were quantified using the Typhoon Imager. ^{35}S-Met/Cys incorporation was quantified for each time point. ^{35}S-Met/Cys incorporation was set to 100% for t = 0 after the 20 min pulse, and the different chase times were expressed relative to this (results are mean SD, n = 5 independent experiments). **c**. Cells were incubated with 1 μM of Palmostatin B for different times at 37°C, lysed, subjected to SDS-PAGE, and analyzed by immunoblotting with anti-myc antibodies. **d**. Thermal denaturation profiles of WT APT2 protein alone or associated with liposomes (interface 1 of sucrose gradient) as monitored by circular dichroism at 222 nm. The temperature of the samples was increased from 4°C to 94°C by 2°C intervals. The normalized ellipticity at 222 nm is plotted against temperature, results are mean SD, n = 3 technical replicates. **e**. The levels of APT1 and 2 mRNA were determined by qPCR upon silencing of APT1 or 2, or various ZDHHC genes.

Europe PMC Funders Author Manuscripts

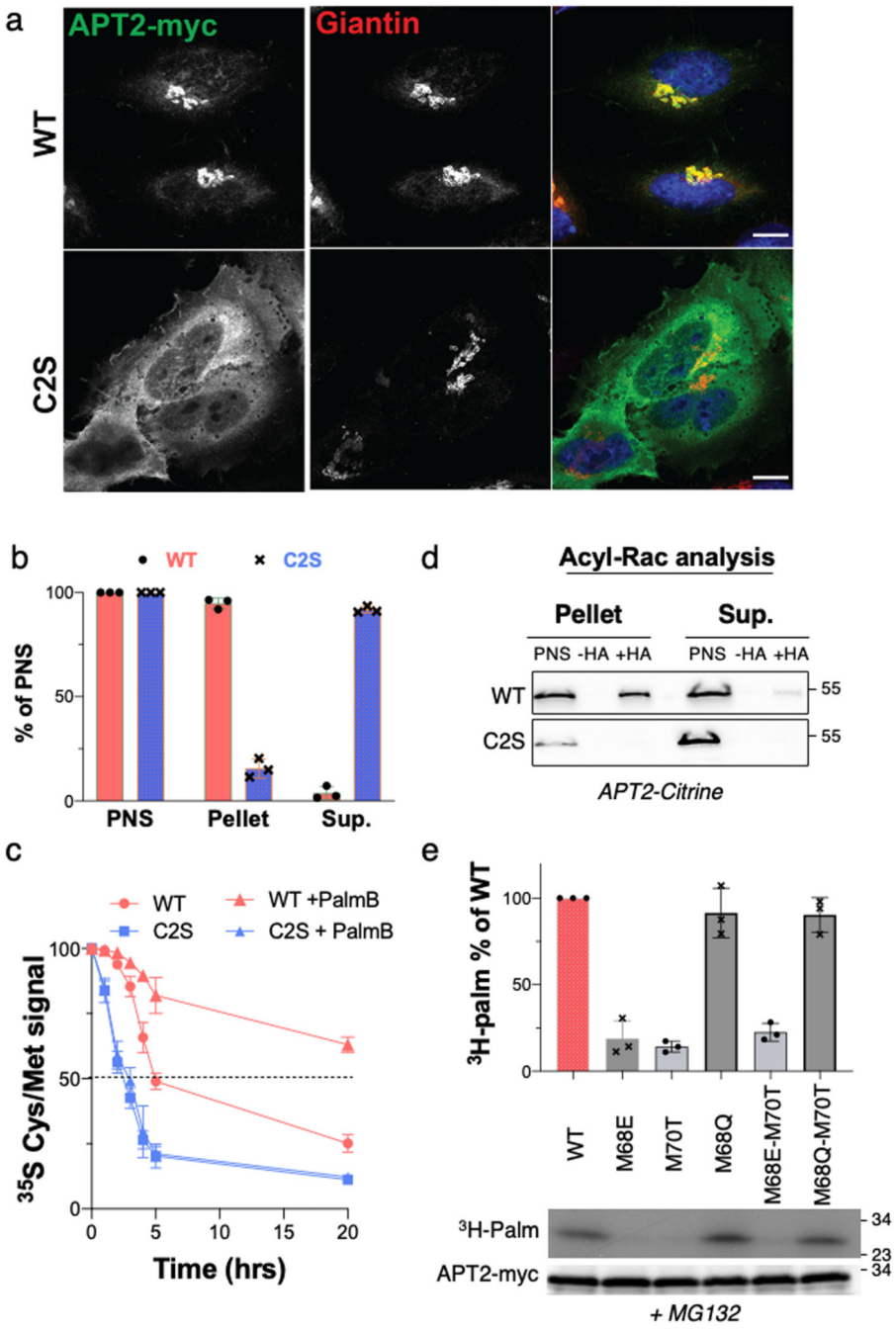

Extended Data Figure 3. Effect of S-acylation on APT2 localization and stability.

a-e : HeLa cells were transfected with plasmids encoding WT or C2S APT2 for 24 h. **a.** Confocal microscopy images of cells expressing WT or C2S APT2-myc immunolabeled for APT2 and Giantin. Nuclei were stained with Hoechst. Scale bar: 10 μm. **b.** PNSs were prepared and ultra-centrifuged to separate the membrane (Pellet) and cytosolic (Sup.) fractions. Equal volumes were analyzed by SDS-PAGE. APT2 WT or C2S levels in each fraction were normalized to that in the PNS (results are mean SD, n = 3 independent experiments). **c.** Cells expressing APT2-myc constructs were treated or not for 4 h with

Palmostatin B, pulsed with ^{35}S Cys/Met for 20 min and then chased for the indicated time before immunoprecipitation and SDS-PAGE. ^{35}S-Met/Cys levels were determined for each time point by autoradiography and quantified using the Typhoon Imager. ^{35}S-Met/Cys levels were normalized to that at t = 0 after the 20-min pulse (results are mean SD, n = 3 independent experiments). **d.** PNS were prepared from cells expressing WT or C2S APT2-myc and ultra-centrifuged to separate membrane (Pellet) and cytosolic (Sup.) fractions. The amount of palmitoylated protein was determined using Acyl-RAC. For each fraction, palmitoylated proteins were detected after hydroxylamine treatment (+HA). Equal volumes were by analyzed SDS-PAGE and immunoblotting with anti-GFP antibodies. **e.** Cells were treated for 4 h with MG132 and were then metabolically labeled for 3 h at 37°C with ^{3}H-palmitic acid. The proteins were extracted, immunoprecipitated with anti-myc antibodies, separated via SDS-PAGE, and analyzed by autoradiography (^{3}H-palm), which was quantified using the Typhoon Imager or by immunoblotting with anti-myc antibodies. The calculated value of ^{3}H-palmitic acid incorporation into WT APT2 was set to 100%, and mutants were expressed relative to this (results are mean SD, n = 3 independent experiments).

Europe PMC Funders Author Manuscripts

Europe PMC Funders Author Manuscripts

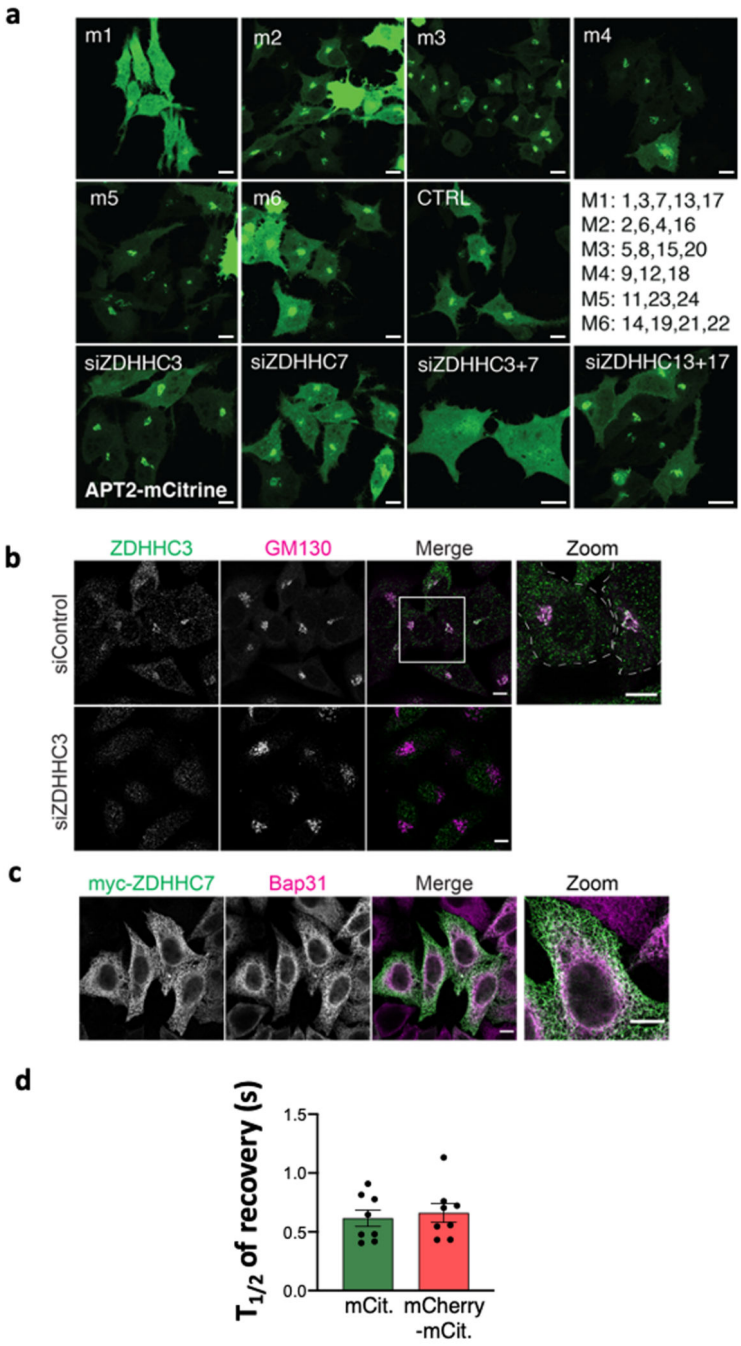

Extended Data Figure 4. Identification of the APT2 acyltransferases.

a. HeLa cells were silenced for 3 days with individual or mixed pools of ZDHHC RNAi transfected with plasmids encoding citrine-tagged WT APT2. Cells were immunolabeled for citrine-APT2 (green). Bar 10 μM**. b**. HeLa cells, silenced for 3 days using a control siRNA or an siRNA against ZDHHC3 were immunolabeled against endogenous ZDHHC3 or the Golgi marker GM130. Bar 10 μM. **c**. HeLa cells expressing myc-ZDHHC7 were immunostained against myc and the ER marker Bap31. Bar: 10 μM. **d.** The kinetics of recovery after photobleaching were determined for cytosolically expressed mCitrine (~27

kDa) and mCherry-mCitrine (~55 kDa). $T_{1/2}$ were computed from FRAP curves using non-linear regression assuming one-phase association. Results are mean SEM, n = 8 independent experiments. The recovery time was not affected by the molecular weight difference.

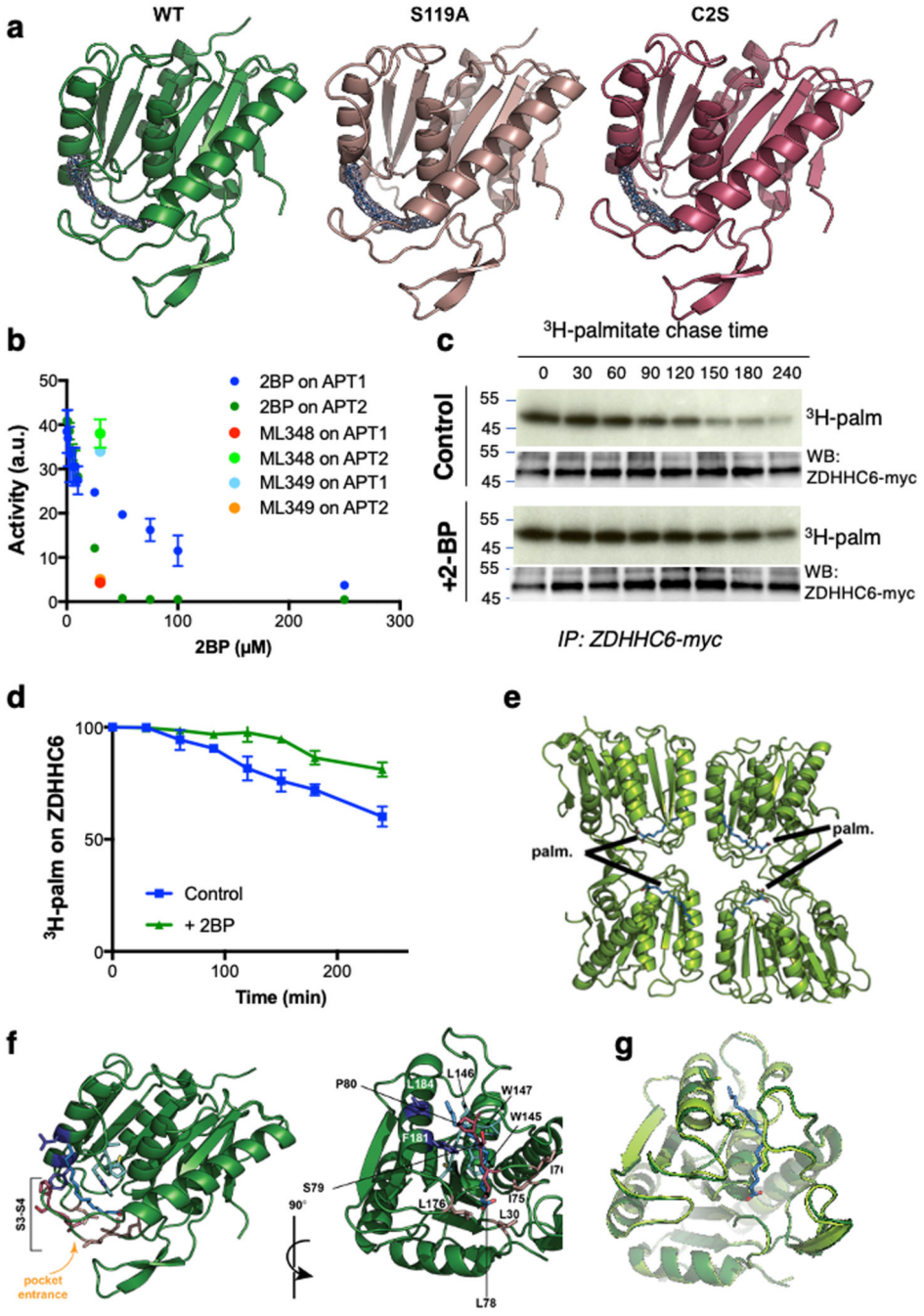

Extended Data Figure 5. Palmitate binding in the APT hydrophobic pocket.

a. Ribbon diagrams of APT1 WT and mutants showing the palmitate moiety in blue into the catalytic pocket with the Fo-Fc map in grey mesh. **b.** APT1 WT showing the 2-bromopalmitate (2-BP) moiety in yellow into the catalytic pocket with the Fo-Fc map in

Europe PMC Funders Author Manuscripts

grey mesh. The Br Fo-Fc is displayed with a red mesh. In the dashed circle a zoom in of the 2-BP orientation with the relative anomalous density map in red mesh. **b.** Determination of the effect of 2-BP on the thioesterase activity of WT APT1 and WT APT2 at 60 min after the addition of substrate and detergent. APT1-specific inhibitor ML348 or APT2-specific inhibitor ML349 at 10 μM were included as positive and negative controls, results are mean SD, n = 3 technical replicates. **cd.** HeLa cells were transfected with plasmids encoding myc-tagged WT ZDHHC6 constructs for 24 h. Cells were metabolically labeled for 2 h at 37°C with ^{3}H-palmitic acid and were chased for different times in new complete medium in the presence or not of 2-BP only during the chase. Proteins were extracted, immunoprecipitated with anti-myc antibodies, subjected to SDS-PAGE, analyzed by autoradiography (^{3}H-palm), and quantified using the Typhoon Imager or by immunoblotting with anti-myc antibodies. ^{3}H-palmitic acid incorporation was set to 100% for cells after the pulse, and values obtained after different chase times were expressed relative to this (results are mean SD, n = 3 independent experiments). **e.** 2-bromopalmitate was bound in all APT1 subunits in the asymmetric unit. Ribbon diagram of the 2-BP/APT1 asymmetric unit. The 2-BP molecules are shown in sticks. **g.** Ribbon diagram of the side (left) and front (right) view of the APT1 enzyme. The residues forming the binding pocket are shown in sticks representation: in red the residues forming the entrance of the pocket, in blue the residues composing the top of the pocket and in light-blue the residues defining the end of the pocket. The rest of the channel is formed by the residues in pink. The entrance of the channel is solvent-exposed and indicated with an orange arrow. The palmitic acid is shown as blue sticks. **g.** Ribbon diagram of the front view of the apo WT APT1 enzyme (light-green) and palmitate-bounded WT APT1 enzyme (dark-green). In sticks representation, the residues involved in the regulation of the lipid access: Leu184, Phe181, and Leu78.

Europe PMC Funders Author Manuscripts

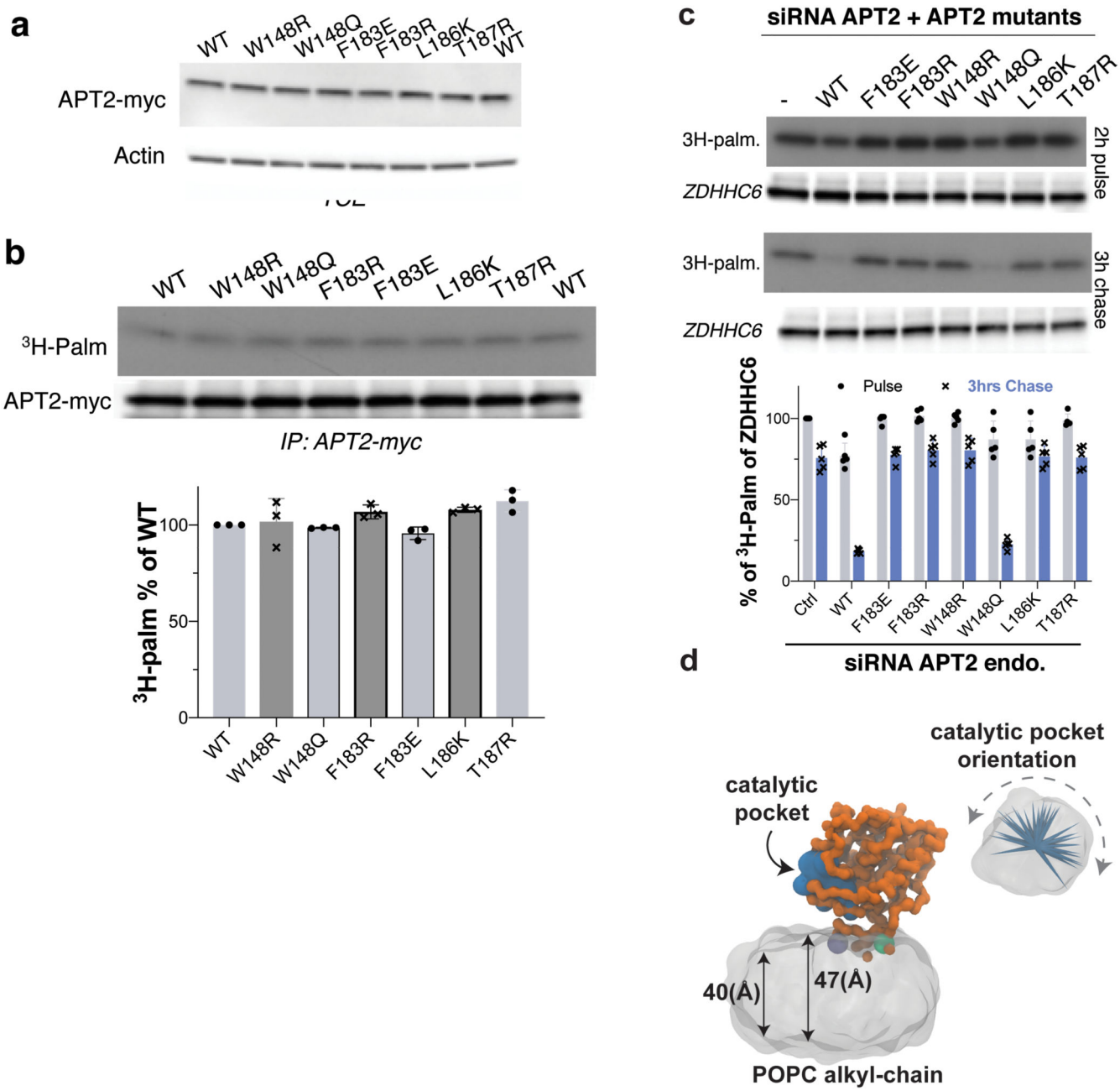

Extended Data Figure 6. The APT2 hydrophobic pocket is essential for activity.

a. Level of expression of APT2 pocket mutants. Total cell extract (TCE) from cells expressing WT or mutant APT2 for 24 h were subjected to SDS-PAGE, and analyzed by immunoblotting with anti-myc antibodies. Anti-actin antibodies were used as a loading control. **b**. HeLa cells were transfected 24h with plasmids encoding the indicated APT2 constructs. Cells were then metabolically labeled for 2 h at 37°C with ^{3}H-palmitic acid. APT2 was immunoprecipitated with anti-myc antibodies, subjected to SDS-PAGE, immunoblotted with anti-myc antibodies, and analyzed by autoradiography (^{3}H-palm). Quantification of the ^{3}H-palmitic acid incorporation into different APT2 mutants. The

calculated value of ^{3}H-palmitic acid incorporation into WT APT2 was set to 100%, and the mutants were expressed relative to this (results are mean SD, n = 3 independent experiments). **c**. ZDHHC6 palmitoylation upon overexpression of APT2 pocket mutants. HeLa cells were silenced for 3 days with APT2 RNAi and were transfected with plasmids encoding myc-tagged WT ZDHHC6 and the indicated APT2 constructs for 24 h. The cells were then metabolically labeled for 2 h at 37°C with ^{3}H-palmitic acid and were chased for 3 h. Proteins were extracted, immunoprecipitated with anti-myc antibodies, separated via SDS-PAGE, immunoprecipitated with anti-myc antibodies, and analyzed by autoradiography (^{3}H-palm). The total extracts (40 μg) were immunoblotted with anti-myc antibodies to determine the expression level of WT and mutant APT2. The calculated value of ^{3}H-palmitic acid incorporation into ZDHHC6 with WT APT2 was set to 100%, and the mutants were expressed relative to this (results are mean SD, n = 3 independent experiments). **d**. Representative snapshot of the membrane-bound APT2 state. In orange, the APT2 protein. The catalytic pocket is shown as blue surface, and the membrane bilayer in grey.

Supplementary Material

Refer to Web version on PubMed Central for supplementary material.

Acknowledgments

We thank Davide Demurtas and Graham Knott from the BioEM EPFL Core Facility for the EM analysis, Stefania Vossio and Dr. Dimitri Moreau from the ACCESS Geneva screening platform; Laure Menin from EPFL ISIC proteomic facility and the beamline scientists of X06DA at SLS (Villigen Switzerland). We thank all the members of the F.G.v.d.G. lab for their discussions and suggestions. This work was supported by the Swiss National Science Foundation, the Swiss National Centre of Competence in Research (NCCR) Chemical Biology, and the European Research Council under the European Union's Seventh Framework Programme (FP/2007-2013) / ERC Grant Agreement n. 340260 - PalmERa'.

Data Availability Statement

Coordinates and structure factors were deposited in the Protein Data Bank (wwPDB) with accession codes: 6QGS for WT/hAPT1; 6QGQ for C2S/hAPT1; 6QGO for S119A/hAPT1; and 6QGN for the 2Br-PLM-C2S/hAPT1 complex.

References

1. Khoury GA, Baliban RC, Floudas CA. Proteome-wide post-translational modification statistics: frequency analysis and curation of the swiss-prot database. Sci Rep. 2011; 1
2. Blanc M, David FPA, van der Goot FG. SwissPalm 2: Protein S-Palmitoylation Database. Methods Mol Biol. 2019; 2009:203–214. [PubMed: 31152406]
3. Gadalla MR, Veit M. Toward the identification of ZDHHC enzymes required for palmitoylation of viral protein as potential drug targets. Expert Opinion on Drug Discovery. 2020; 15:159–177. [PubMed: 31809605]
4. Brown RWB, Sharma AI, Engman DM. Dynamic protein S-palmitoylation mediates parasite life cycle progression and diverse mechanisms of virulence. Crit Rev Biochem Mol Biol. 2017; 52:145–162. [PubMed: 28228066]
5. Zaballa M-E, van der Goot FG. The molecular era of protein S-acylation: spotlight on structure, mechanisms, and dynamics. Crit Rev Biochem Mol Biol. 2018; 53:420–451. [PubMed: 29999430]

6. Duncan JA, Gilman AG. A cytoplasmic acyl-protein thioesterase that removes palmitate from G protein alpha subunits and p21(RAS). The Journal of biological chemistry. 1998; 273:15830–7. [PubMed: 9624183]
7. Tomatis VM, Trenchi A, Gomez GA, Daniotti JL. Acyl-protein thioesterase 2 catalyzes the deacylation of peripheral membrane-associated GAP-43. PLoS ONE. 2010; 5
8. Zingler P, et al. Palmitoylation is required for TNF-R1 signaling. Cell Commun Signal. 2019; 17
9. Chen S, et al. Targeting MC1R depalmitoylation to prevent melanomagenesis in redheads. Nat Commun. 2019; 10:877. [PubMed: 30787281]
10. Abrami L, et al. Identification and dynamics of the human ZDHHC16-ZDHHC6 palmitoylation cascade. eLife. 2017; 6
11. Conibear E, Davis NG. Palmitoylation and depalmitoylation dynamics at a glance. Journal of cell science. 2010; 123:4007–10. [PubMed: 21084560]
12. Fukata Y, Murakami T, Yokoi N, Fukata M. Local Palmitoylation Cycles and Specialized Membrane Domain Organization. Current topics in membranes. 2016; 77:97–141. [PubMed: 26781831]
13. Lemonidis K, et al. The zDHHC family of S-acyltransferases. Biochemical Society transactions. 2015; 43:217–21. [PubMed: 25849920]
14. Salaun C, Greaves J, Chamberlain LH. The intracellular dynamic of protein palmitoylation. J Cell Biol. 2010; 191:1229–38. [PubMed: 21187327]
15. Lin DT, Conibear E. Enzymatic protein depalmitoylation by acyl protein thioesterases. Biochemical Society transactions. 2015; 43:193–8. [PubMed: 25849916]
16. Won SJ, Cheung See Kit M, Martin BR. Protein depalmitoylases. Critical reviews in biochemistry and molecular biology. 2018; 53:83–98. [PubMed: 29239216]
17. Kong E, et al. Dynamic palmitoylation links cytosol-membrane shuttling of acyl-protein thioesterase-1 and acyl-protein thioesterase-2 with that of proto-oncogene H-ras product and growth-associated protein-43. The Journal of biological chemistry. 2013; 288:9112–25. [PubMed: 23396970]
18. Vartak N, et al. The Autodepalmitoylating Activity of APT Maintains the Spatial Organization of Palmitoylated Membrane Proteins. Biophysical journal. 2014; 106:93–105. [PubMed: 24411241]
19. Shahinian S, Silvius JR. Doubly-lipid-modified protein sequence motifs exhibit long-lived anchorage to lipid bilayer membranes. Biochemistry. 1995; 34:3813–3822. [PubMed: 7893678]
20. Won SJ, et al. Molecular Mechanism for Isoform-Selective Inhibition of Acyl Protein Thioesterases 1 and 2 (APT1 and APT2). ACS chemical biology. 2016; 11:3374–3382. [PubMed: 27748579]
21. Devedjiev Y, Dauter Z, Kuznetsov SR, Jones TL, Derewenda ZS. Crystal structure of the human acyl protein thioesterase I from a single X-ray data set to 1.5 A. Structure. 2000; 8:1137–46. [PubMed: 11080636]
22. Wepy JA, et al. Lysophospholipases cooperate to mediate lipid homeostasis and lysophospholipid signaling. J Lipid Res. 2019; 60:360–374. [PubMed: 30482805]
23. Duarte JM, Srebniak A, Schärer MA, Capitani G. Protein interface classification by evolutionary analysis. BMC Bioinformatics. 2012; 13:334. [PubMed: 23259833]
24. Mueller M, Grauschopf U, Maier T, Glockshuber R, Ban N. The structure of a cytolytic alpha-helical toxin pore reveals its assembly mechanism. Nature. 2009; 459:726–30. [PubMed: 19421192]
25. Kathayat RS, et al. Active and dynamic mitochondrial S-depalmitoylation revealed by targeted fluorescent probes. Nat Commun. 2018; 9:334. [PubMed: 29362370]
26. Fukata Y, Fukata M. Protein palmitoylation in neuronal development and synaptic plasticity. Nat Rev Neurosci. 2010; 11:161–75. [PubMed: 20168314]
27. Ohno Y, Kihara A, Sano T, Igarashi Y. Intracellular localization and tissue-specific distribution of human and yeast DHHC cysteine-rich domain-containing proteins. Biochim Biophys Acta. 2006; 1761:474–83. [PubMed: 16647879]
28. Ernst AM, et al. S-Palmitoylation Sorts Membrane Cargo for Anterograde Transport in the Golgi. Dev Cell. 2018; 47:479–493.e7. [PubMed: 30458139]

29. Ngaki MN, et al. Evolution of the chalcone-isomerase fold from fatty-acid binding to stereospecific catalysis. Nature. 2012; 485:530–533. [PubMed: 22622584]
30. Pedro MP, et al. 2-Bromopalmitate reduces protein deacylation by inhibition of acyl-protein thioesterase enzymatic activities. PLoS ONE. 2013; 8
31. Rocks O, et al. The palmitoylation machinery is a spatially organizing system for peripheral membrane proteins. Cell. 2010; 141:458–471. [PubMed: 20416930]
32. Pedro MP, Vilcaes AA, Gomez GA, Daniotti JL. Individual S-acylated cysteines differentially contribute to H-Ras endomembrane trafficking and acylation/deacylation cycles. Mol Biol Cell. 2017; 28:962–974. [PubMed: 28179458]
33. Hernandez JL, et al. APT2 Inhibition Restores Scribble Localization and S-Palmitoylation in Snail-Transformed Cells. Cell Chem Biol. 2017; 24:87–97. [PubMed: 28065656]
34. Lakkaraju AK, et al. Palmitoylated calnexin is a key component of the ribosome-translocon complex. Embo J. 2012; 31:1823–1835. [PubMed: 22314232]
35. Kemp LE, et al. Characterization of a serine hydrolase targeted by acyl-protein thioesterase inhibitors in Toxoplasma gondii. The Journal of biological chemistry. 2013; 288:27002–18. [PubMed: 23913689]
36. Kabsch WXDS. Acta Crystallogr D Biol Crystallogr. 2010; 66:125–132. [PubMed: 20124692]
37. Emsley P, Cowtan K. Coot: model-building tools for molecular graphics. Acta Crystallogr D Biol Crystallogr. 2004; 60:2126–32. [PubMed: 15572765]
38. Echols N, et al. Graphical tools for macromolecular crystallography in PHENIX. J Appl Crystallogr. 2012; 45:581–586. [PubMed: 22675231]
39. Klauda JB, et al. Update of the CHARMM all-atom additive force field for lipids: validation on six lipid types. J Phys Chem B. 2010; 114:7830–7843. [PubMed: 20496934]
40. Phillips JC, et al. Scalable molecular dynamics with NAMD. J Comput Chem. 2005; 26:1781–802. [PubMed: 16222654]
41. Darden T, York D, Pedersen L. Particle mesh Ewald: An N·log(N) method for Ewald sums in large systems. J Chem Phys. 1993; 98:10089–10092.
42. Marrink SJ, Risselada HJ, Yefimov S, Tieleman DP, de Vries AH. The MARTINI force field: coarse grained model for biomolecular simulations. J Phys Chem B. 2007; 111:7812–7824. [PubMed: 17569554]
43. Abraham MJ, et al. GROMACS: High performance molecular simulations through multi-level parallelism from laptops to supercomputers. SoftwareX. 2015; 1-2:19–25.
44. Werno MW, Chamberlain LH. S-acylation of the Insulin-Responsive Aminopeptidase (IRAP): Quantitative analysis and Identification of Modified Cysteines. Scientific reports. 2015; 5
45. Rueden CT, et al. ImageJ2: ImageJ for the next generation of scientific image data. BMC Bioinformatics. 2017; 18:529. [PubMed: 29187165]

Europe PMC Funders Author Manuscripts

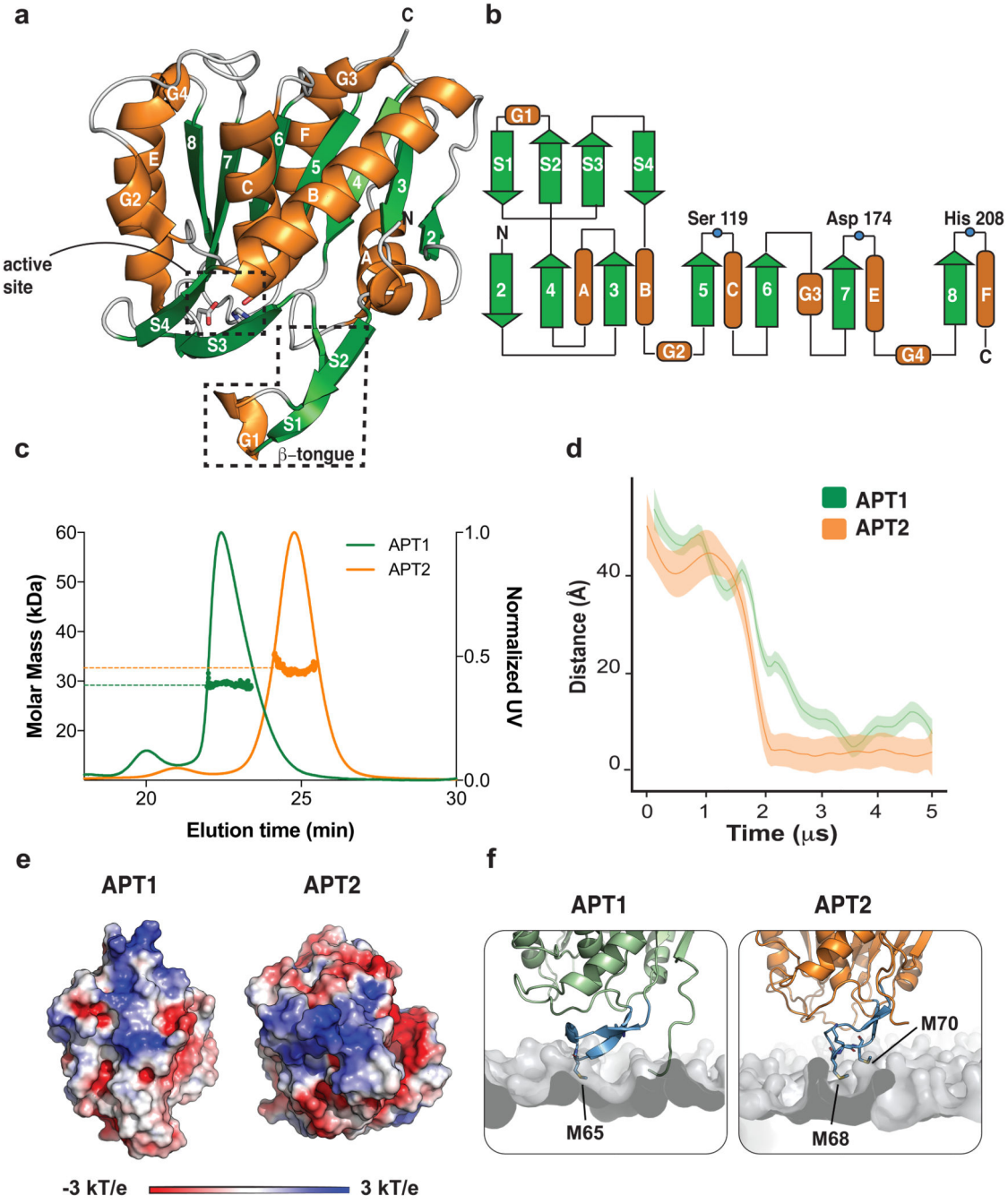

Figure 1. Structure and membrane interaction of APTs,

a. Ribbon diagram of APT1 (PDB id: 1FJ2), with β strands in green arrows and helices in orange. An insertion atypical of the α/β hydrolase is boxed. The catalytic active site and the β-tongue are contoured in black. **b.** Topology of the APT enzymes (APT1 residue numbering is used). **c.** SEC-MALS analysis of APT1 and APT2. **d.** Distance plot monitoring APT1 (green) and APT2 (orange) membrane interaction over the MD simulation time. The published APT2 structure (PDB id 5SYN) was used in the MD analyses [20]. n = 5 independent MD replicas were considered for both APT1 and APT2 systems. The filled

colors represent the 95% confidence level interval for APT1 (green) and APT2 (orange) distance measurements. **e.** Electrostatic surface potential of APT1 (left) and APT2 (right) shows the highly positive surface (blue) on the surface. **f.** Close-up view of the enzyme-protein interaction for APT1 (left) and APT2 (right). The β-tongue is highlighted in blue. The side chains of the residues involved in the membrane interaction are shown as blue sticks.

Europe PMC Funders Author Manuscripts

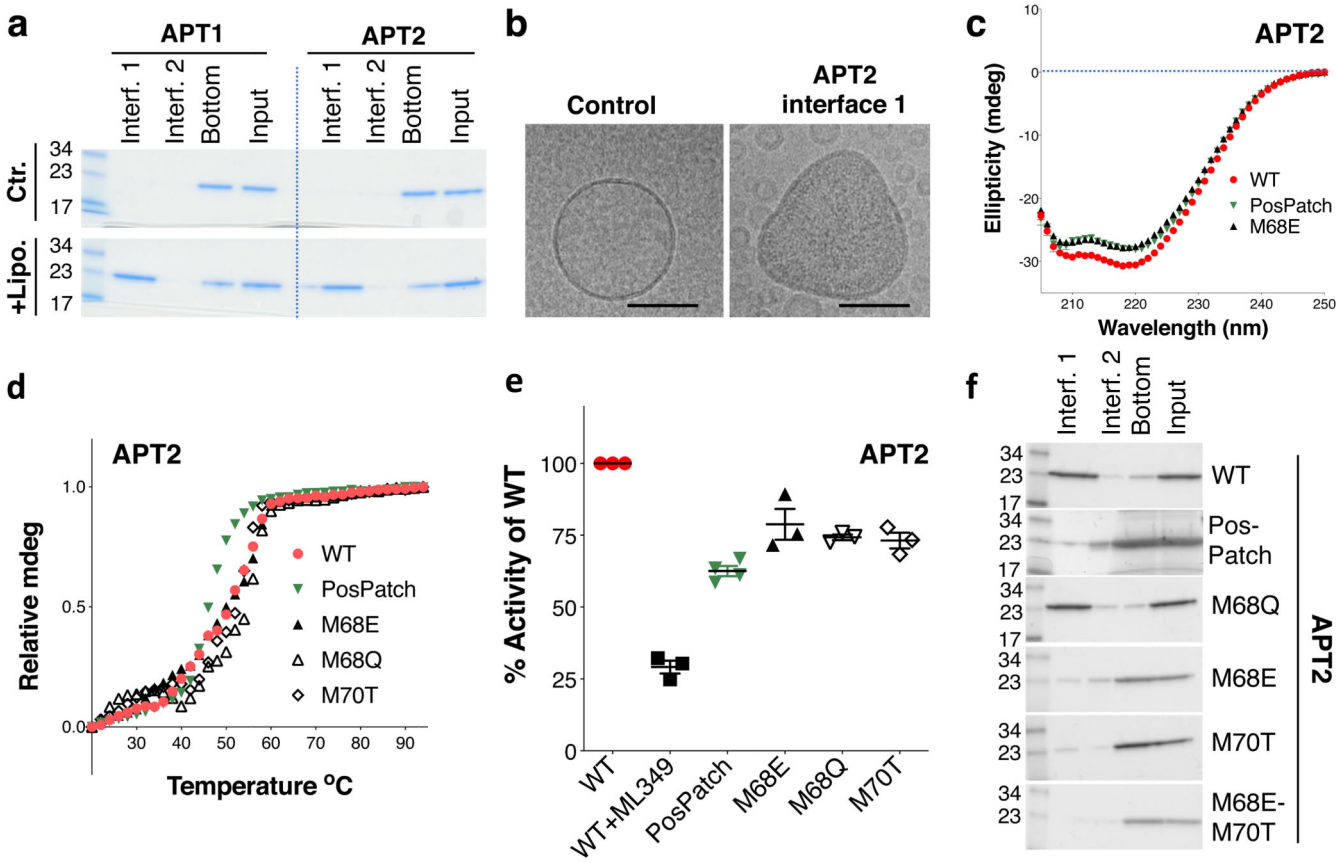

Figure 2. Membrane binding of APTs.

a. Purified WT APT1 and APT2 protein were incubated with liposomes and applied to the bottom of a step sucrose gradient. The interfaces were collected from top to bottom, loaded on an SDS-PAGE gel, and stained with Coomassie blue. **b.** Interface 1 (Interf. 1) for APT2-loaded liposomes was analyzed by negative staining and cryo EM. Bar = 100 μm. **c.** Circular dichroism spectra of WT APT2, the Positive Patch (PosPatch:H38A-H58A-R61A-K69A-K94A) and the ß tongue M68E mutants. **d.** Thermal denaturation profiles of WT APT2, the PosPatch or the ß tongue mutants as monitored by circular dichroism at 222 nm. The normalized ellipticity at 222 nm is plotted against temperature. **e.** The thioesterase activity of WT APT2, the PosPatch or the ß tongue mutants was determined at 60 min after the addition of substrate and detergent. APT2-specific inhibitor ML349 was included as a positive control. Technical replicates were averaged within each experiment, and each experiment was normalized to WT. Two-tailed two-sample unequal variance t-tests were performed on the raw values normalized to the plate (n = 3 independent experiments, except PosPastch n = 4). **f.** WT and different APT2 mutants were incubated with liposomes and applied to the bottom of a sucrose gradient. The different interfaces from the top to bottom were collected and loaded on an SDS-PAGE and stained with Coomassie blue.

Europe PMC Funders Author Manuscripts

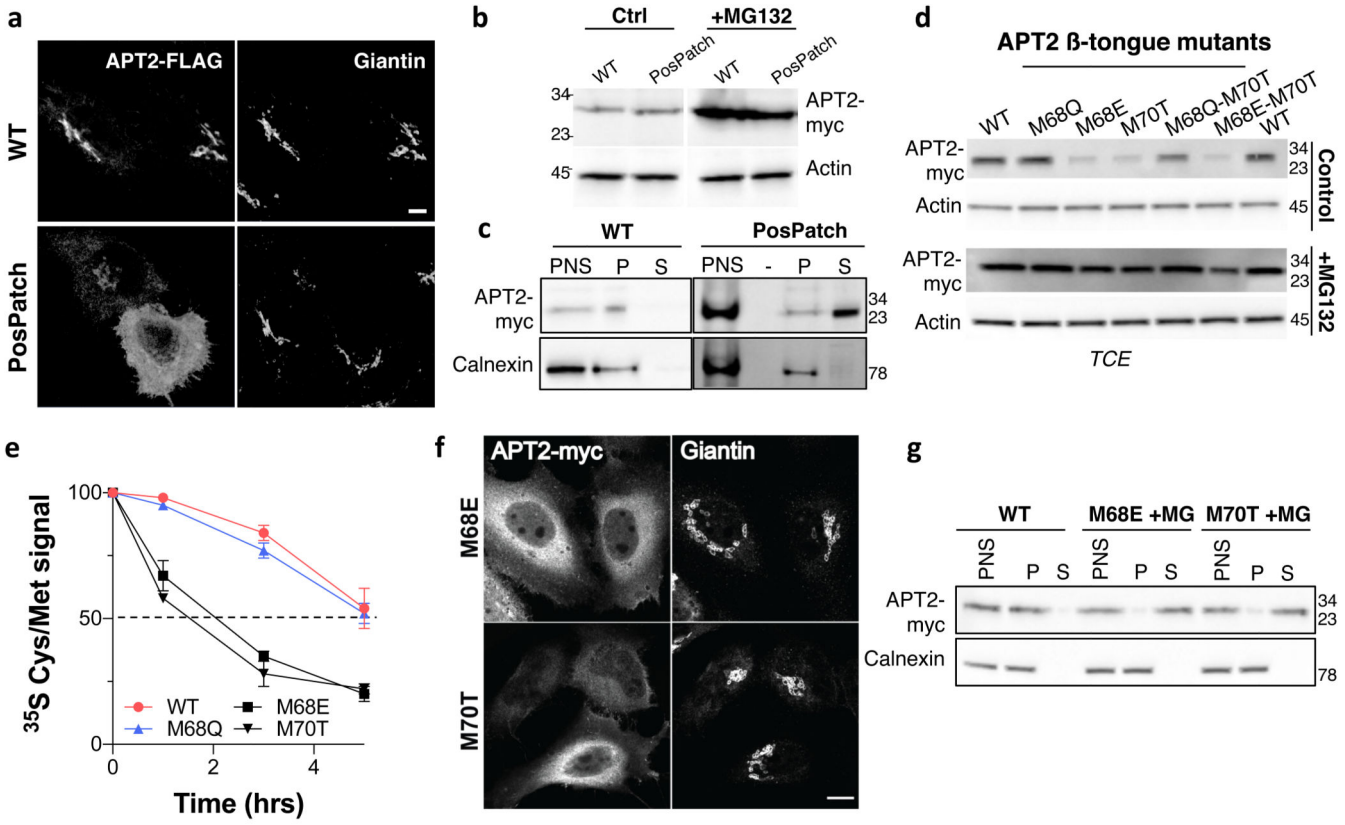

Figure 3. Cellular expression and distribution of APT2 PosPatch and ß tongue mutants.

a. Confocal microscopy images of HeLa cells transfected with plasmids encoding APT2-myc WT or Positive Patch (PosPatch: H38A-H58A-R61A-K69A-K94A) for 24 h. Cells were immunolabeled for APT2-myc and Giantin, as Golgi marker. Scale bar: 10 μm. **b.** HeLa cells expressing WT or the PosPatch APT2 mutant for 24 h were incubated or not for 4 h with MG132. Protein extracts (40 μg) were separated via SDS-PAGE and analyzed by immunoblotting with anti-myc antibodies. Actin was used as a loading control. **c.** HeLa cells were transfected with plasmids encoding WT or PosPatch mutant APT2-myc for 24 h. Post-nuclear supernatants (PNS) were prepared and ultra-centrifuged to separate membrane (P) from cytosolic (S) fractions. Equal volumes were loaded on a 4–20% gradient SDS-PAGE gel and were analyzed by immunoblotting with anti-myc and anti-Calnexin antibodies. **d**. HeLa cells expressing WT or mutant APT2-myc for 24 h were incubated or not for 4 h with MG132 and analyzed as in **b**. **e.** HeLa cells were transfected with different APT2-myc constructs for 24 h. Cells were pulsed with ^{35}S Cys/Met for 20 min and chased for the indicated time before immunoprecipitation and SDS-PAGE. Degradation kinetics were analyzed by autoradiography and were quantified using the Typhoon Imager. ^{35}S-Met/Cys incorporation was quantified for each time point and was normalized to protein expression levels. ^{35}S-Met/Cys incorporation was set to 100% for t = 0, and all chase times were expressed relative to this (results are mean/SD, n = 3 independent experiments). **f.** Confocal microscopy images of HeLa cells transfected with plasmids encoding APT2-myc mutants for 24 h. Cells were incubated for 4 h with MG132 and were immunolabeled for APT2-myc and Giantin, as Golgi marker. Scale bar: 10 μm. **g.** HeLa cells were transfected with

plasmids encoding WT or mutant APT2-myc for 24 h. Where applicable, cells were incubated for 4 h with MG132. PNS were prepared and analyzed as in **c**.

Europe PMC Funders Author Manuscripts

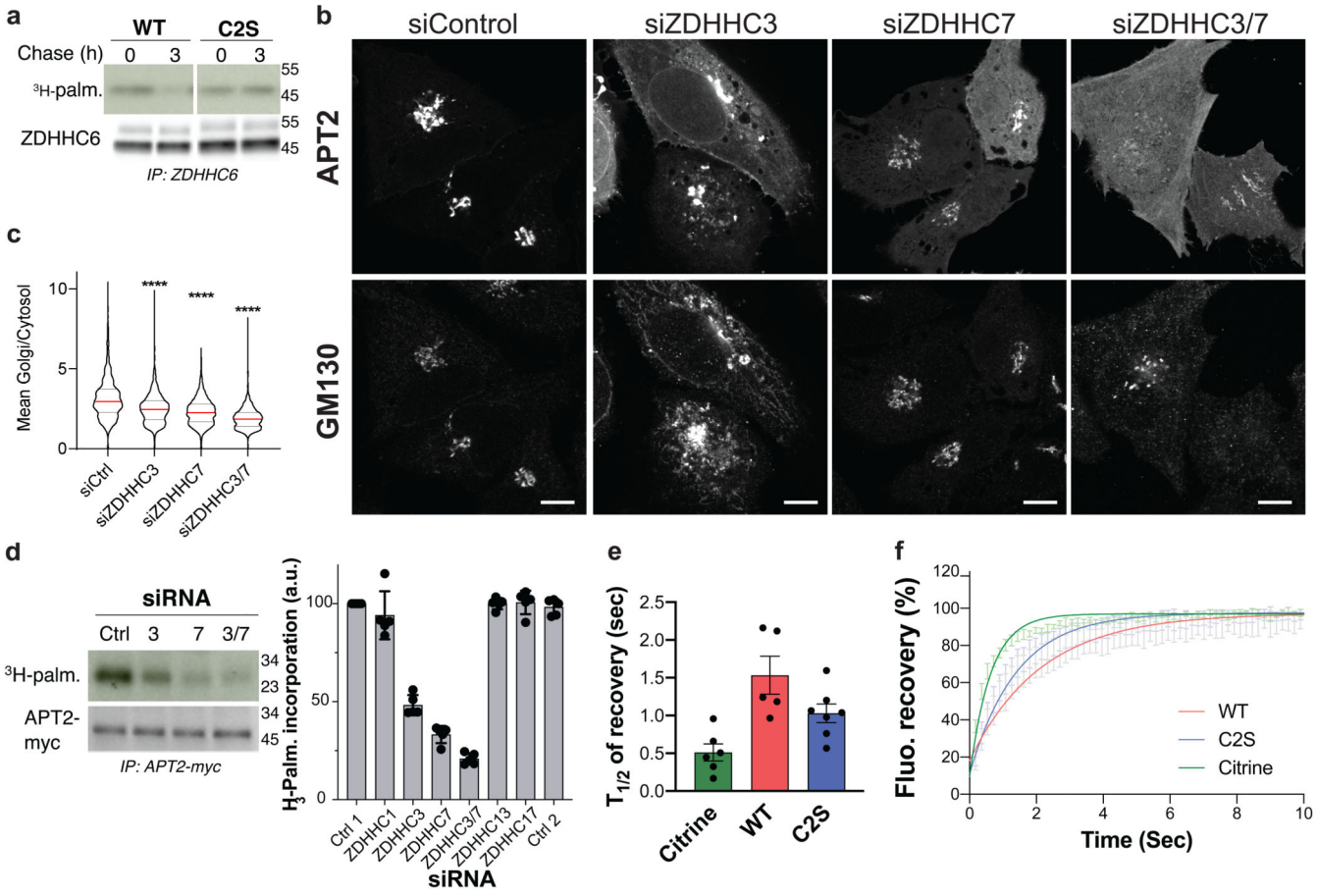

Figure 4. ZDHHCs 3 and 7-mediated APT2 S-acylation and the effect on activity.

a. HeLa cells were silenced for 3 days with APT2 RNAi and transfected with plasmids encoding myc-tagged WT ZDHHC6 and APT2 WT or C2S for 24 h. The cells were then metabolically labeled for 2 h at 37°C with ^{3}H-palmitic acid and chased for 3 h in free medium. Proteins were extracted, immunoprecipitated with anti-myc antibodies, subjected to SDS-PAGE, and analyzed by autoradiography (^{3}H-palm) or by immunoblotting with anti-myc antibodies. **b.** Confocal microscopy images of HeLa cells transfected with siRNAs against ZDHHC3, 7, or both, plasmids encoding APT2-citrine for 24h, and immunolabelled for GM130. Scale bar: 10 μm. **c.** High-throughput automated immunofluorescence quantification of HeLa cells processed as in **b**, depicting the ratio of APT2 mean intensity values between the Golgi (marked by GM130) and the cytosol (cell mask without nuclei and Golgi). Violin plots show the frequency distribution of all values within a representative experiment with median (red line) and quartiles (black lines). n = 1920, siCtr; 1856, siZDHHC3; 2333, siZDHHC7; 2140, siZDHHC3/7 and *p* values were obtained by One-way ANOVA with Tiukey's multiple comparison test (p****<0.0001). Equivalent results were obtained for two independent analyses. **d**. HeLa cells were transfected with siRNAs against ZDHHC3, 7 or both and a plasmid encoding APT2-myc, then metabolically labeled for 2 h at 37°C with ^{3}H-palmitic acid. Proteins were extracted, immunoprecipitated with anti-myc antibodies, subjected to SDS-PAGE, and analyzed by autoradiography (^{3}H-palm) or by immunoblotting with anti-myc antibodies (results are meanHSD, n = 5 independent

Europe PMC Funders Author Manuscripts

experiments). **ef.** Fluorescence recovery after photobleaching curves for APT2 WT and palmitoylation deficient C2S mutant. The recovery within a bleached region chosen outside of the Golgi area was followed for 20 s at 180 ms intervals and expressed as percentage relative to prebleach fluorescence value of the region (**f**). Data were fit using non-linear regression. Half-time of recovery ($t_{1/2}$) was defined as the time required to achieve half of the maximum fluorescence value, was computed using one-phase association equation (**e**). Results are mean)SEM, n = 6 independent experiments.

Europe PMC Funders Author Manuscripts

Europe PMC Funders Author Manuscripts

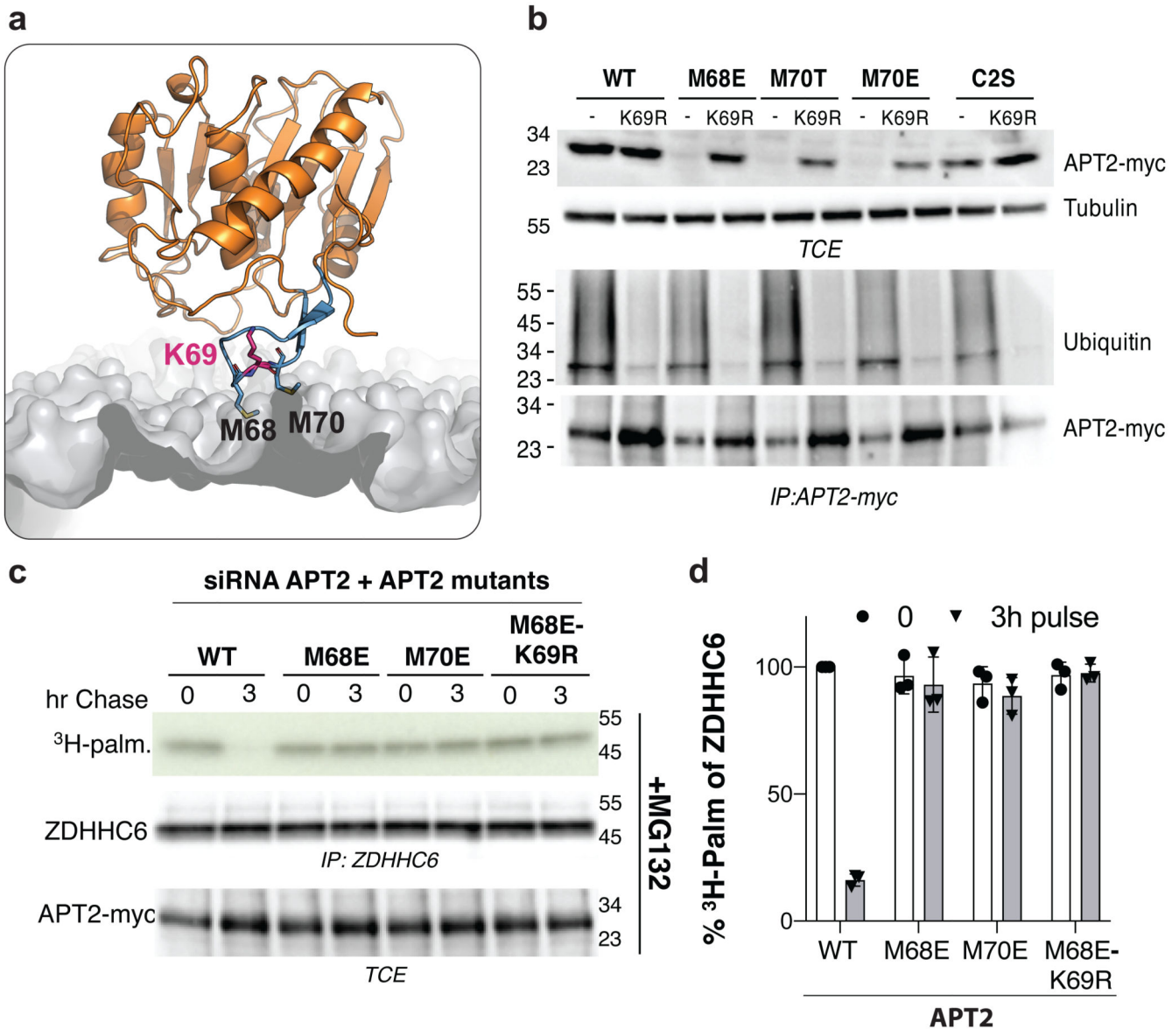

Figure 5. APT2 ß tongue mutants undergo ubiquitination on Lys-69.

a. Ribbon diagram of membrane-bound APT2. **b.** HeLa cells expressing WT or mutant APT2 for 24 h were lysed and immunoprecipitated with anti-myc agarose beads overnight. Protein extracts (40 μg) and immunoprecipitated products were separated via SDS-PAGE and analyzed by immunoblotting with anti-myc or anti-ubiquitin antibodies. Tubulin was blotted as a loading control. **c.** HeLa cells were silenced for 3 days with APT2 siRNA and were transfected with plasmids encoding myc-tagged WT ZDHHC6 and the indicated APT2 constructs for 24 h. Cells were incubated for 4 h with MG132, then metabolically labeled for 2 h at 37°C with ^{3}H-palmitic acid and chased for 3 h in fresh medium. Proteins were extracted, immunoprecipitated with anti-myc antibodies, subjected to SDS-PAGE, immunoblotted with anti-myc antibodies, and analyzed by autoradiography (^{3}H-palm). The total extracts (40 μg) were immunoblotted with anti-myc antibodies to detect WT and

mutant APT2. **d.** Quantification of ^{3}H-palmitic acid incorporation into ZDHHC6 in the presence of different APT2 mutants. Values were normalized to protein expression level. The calculated value of ^{3}H-palmitic acid incorporation into ZDHHC6 with WT APT2 was set to 100%, and the mutants were expressed relative to this (results are meaneSD, n = 3 independent experiments).

Europe PMC Funders Author Manuscripts

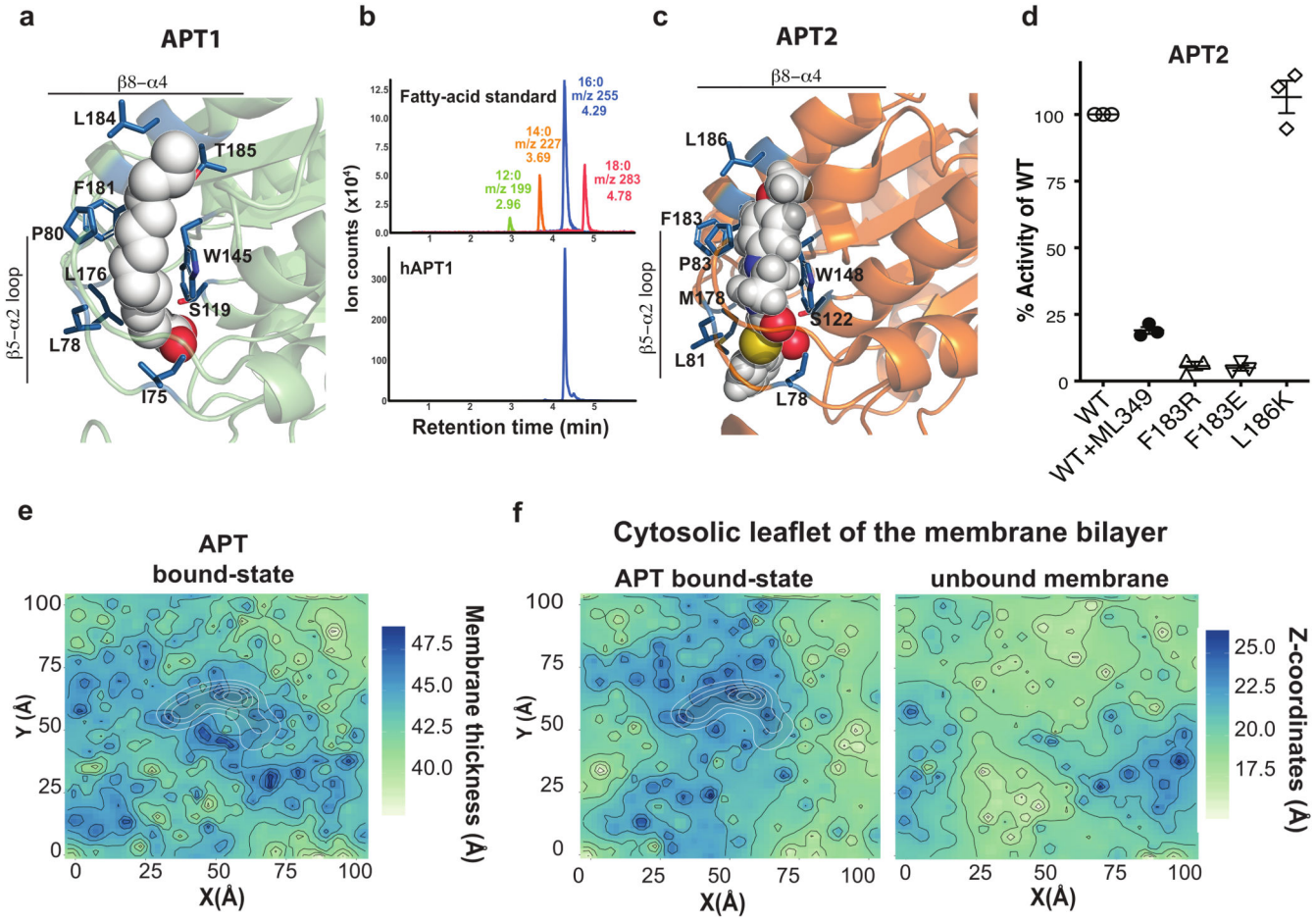

Figure 6. Identification of an acyl chain binding pocket in APTs.

a. Close-up view of the hydrophobic channel of APT1 containing palmitic acid in van der Waals representation. Side-chain of residues forming the hydrophobic cavity are shown as blue sticks. **b**. Analysis of the ligands associated with purified APT1 enzyme detected by Q-TOF-MS. The y-axes represent negative-ion count for selected masses of anion in forms of fatty acid. The top panel depicts the binding of the 4 fatty acid standards: lauric acid (green), myristic acid (orange), palmitic acid (blue) and oleic acid (red). The bottom panel depicts binding of C16:0 by APT1. **c.** Close-up view of the hydrophobic channel of APT2 with ML349 in van der Waals representation. **d**. The thioesterase activity of the APT2 hydrophobic pocket mutants was determined at 60 min after the addition of substrate and detergent. The APT2-specific inhibitor ML349 was included as a positive control. Technical replicates were averaged within each experiment, and each experiment was then normalized to WT. The average of each experiment was graphed. Two-tailed two-sample unequal variance t-tests were performed on the raw values normalized to the plate, results are mean-SD, n = 3 independent experiments. **e.** MD-averaged membrane-thickness. In white is the space explored by the protein during the simulation. **h.** Averaged phosphate Z-coordinates for the APT-bound and APT-unbound states. The dashed line highlights the membrane bound region explored by APT during the simulation.

Europe PMC Funders Author Manuscripts